



1 Inter-comparison of multiple two-way coupled meteorology and air quality models
2 (WRF v4.1.1-CMAQ v5.3.1, WRF-Chem v4.1.1, and WRF v3.7.1-CHIMERE v2020r1)
3 in eastern China

4
5 Chao Gao^{1,2}, Xuelei Zhang^{1,2,*}, Aijun Xiu^{1,2,*}, Qingqing Tong^{1,2}, Hongmei Zhao^{1,2}, Shichun Zhang^{1,2},
6 Guangyi Yang^{1,2,3}, Mengduo Zhang^{1,2,3}, and Shengjin Xie^{1,2,4}

7
8 ¹Key Laboratory of Wetland Ecology and Environment, Northeast Institute of Geography and Agroecology, Chinese
9 Academy of Sciences, Changchun, 130102, China

10 ²Key Laboratory of Wetland Ecology and Environment, State Key Laboratory of Black Soils Conservation and
11 Utilization, Northeast Institute of Geography and Agroecology, Chinese Academy of Sciences, Changchun, 130102,
12 China

13 ³University of Chinese Academy of Sciences, Beijing, 100049, China

14 ⁴School of Environment, Harbin Institute of Technology, 150000, Harbin, China

15 Correspondence to: X.L. Zhang (zhangxuelei@iga.ac.cn) & A.J. Xiu (xiujun@iga.ac.cn)

16 Abstract

17
18 In the eastern China region, two-way coupled meteorology and air quality models
19 have been applied aiming to more realistically simulate meteorology and air quality by
20 accounting for the aerosol–radiation–cloud interactions. There have been numerous
21 related studies being conducted, but the performances of multiple two-way coupled
22 models simulating meteorology and air quality under equivalent configurations have
23 not been compared in this region. In this study, we systematically evaluated annual and
24 seasonal meteorological and air quality variables simulated by three open-source and
25 widely used two-way coupled models (i.e., WRF-CMAQ, WRF-Chem, and WRF-
26 CHIMERE) by validating the model results with surface and satellite observations for
27 eastern China during 2017. Our comprehensive model evaluations showed that all three
28 two-way coupled models simulated the annual spatiotemporal distributions of
29 meteorological and air quality variables reasonably well, especially the surface
30 temperature (with R up to 0.97) and fine particular matter (PM_{2.5}) concentrations (with
31 R up to 0.68). The model results of winter PM_{2.5} and summer ozone compared better
32 with observations and WRF-CMAQ exhibited the best overall performance. The
33 aerosol feedbacks affected model results of meteorology and air quality in various ways
34 and turning on aerosol-radiation interactions made the PM_{2.5} and surface shortwave
35 radiation simulations better, but worse for T2 and Q2. The impacts of aerosol-cloud
36 interactions (ACI) on model performances' improvements were limited and several
37 possible improvements on ACI representations in two-way coupled models are further
38 discussed and proposed. When sufficient computational resources become available,
39 two-way coupled models including the aerosol-radiation-cloud interactions should be
40 applied for more accurate air quality prediction and timely warning of air pollution
41 events in atmospheric environmental management.

42
43
44



45 1 Introduction

46 Aerosols in the atmosphere due to anthropogenic and nature emissions not only
47 cause air pollution but also induce climate and meteorological impacts through aerosol-
48 radiation interaction (ARI) and aerosol-cloud interaction (ACI) (Carslaw et al., 2010;
49 Rosenfeld et al., 2014; Fan et al., 2016; IPCC, 2021). The feedbacks of aerosols to
50 meteorology have been widely investigated by two-way coupled meteorology and air
51 quality models in the past two decades (Jacobson, 2002; Grell et al., 2005; Wong et al.,
52 2012; Wang et al., 2014; Zhou et al., 2016; Briant et al., 2017; Feng et al., 2021). In
53 these models, two-way interactions between meteorology and aerosols are enabled by
54 including all the processes involving ARI or/and ACI (Grell and Baklanov, 2011; Wang
55 et al., 2014; Briant et al., 2017; Wang et al., 2021). The fundamental theories, modeling
56 technics, developments, and applications of two-way coupled meteorology and air
57 quality models in North America, Europe and Asia have been systemically reviewed
58 (Zhang, 2008; Baklanov et al., 2014; Gao et al., 2022).

59 As pointed out by these review papers, the treatments and parameterization
60 schemes of all the physiochemical processes involving ARI and ACI can be very
61 different in two-way coupled models, so that the simulation results from these models
62 could vary in many aspects. At the same time, the configurations of coupled models,
63 such as meteorological and chemical initial and boundary conditions (ICs and BCs),
64 horizontal and vertical resolutions, and emission inventories and processing tools, etc.,
65 play important roles in models' simulations. In the past, model inter-comparison
66 projects have been carried out targeting various two-way coupled meteorology and air
67 quality models. For example, the Air Quality Model Evaluation International Initiative
68 Phase II focused on the performance of multiple two-way coupled models and the
69 effects of aerosol feedbacks in Europe and the United States (Brunner et al., 2015; Im
70 et al., 2015a, b; Makar et al., 2015a, b). In Asia, the Model Inter-Comparison Study for
71 Asia Phase III was conducted to evaluate ozone (O₃) and other gaseous pollutants, fine
72 particular matter (PM_{2.5}), and acid and reactive nitrogen deposition with various models
73 with/out ARI or/and ACI (Li et al., 2019; Chen et al., 2019; Itahashi et al., 2020; Ge et
74 al. al., 2020; Kong et al., 2020). With respect to this project, Gao et al. (2018, 2020)
75 have reviewed in detail the model performance of seven two-way coupled models from
76 different research groups in simulating a heavy air pollution episode during January
77 2010 in North China Plain and how aerosol feedbacks affected simulations of
78 meteorological variables and PM_{2.5} concentrations. Targeting the heavy polluted India
79 region, Govardhan et al. (2016) compared aerosol optical depth (AOD) and various
80 aerosol species (black carbon, mineral dust, and sea salt) modeled by WRF-Chem (with
81 ARI) and Spectral Radiation-Transport Model for Aerosol Species (with both ARI and
82 ACI), but under different model configurations.

83 So far, there is no comprehensive comparisons of multiple coupled models under
84 the same model configuration with respect to the high aerosol loading region over
85 eastern China, where has experienced rapid growth of economy, urbanization,
86 population, as well as severe air quality problems in the past decades (He et al., 2002;
87 Wang and Hao, 2012; Gao et al., 2017; Geng et al., 2021). In the eastern China region
88 (ECR), several open-source and proprietary two-way coupled models have been applied



89 to investigate the ARI and/or ACI effects, yet most studies have focused on certain
90 short-term episodes of heavy air pollution without any year-long simulations (Xing et
91 al., 2017; Ding et al., 2019; Ma et al., 2021). The commonly used open-source models
92 in ECR are WRF-Chem and WRF-CMAQ (Grell et al., 2005; Wong et al., 2012), but
93 there is no any application of the two-way coupled WRF-CHIMERE model that has
94 been applied to examine aerosol-radiation-cloud interactions in Europe and Africa
95 (Briant et al., 2017; Tuccella et al., 2019). At the same time, model simulations should
96 be compared not only against surface measurement data but also satellite data (Zhao et
97 al., 2017; Hong et al., 2017; Campbell et al., 2017; Wang et al., 2018). Even though the
98 running time of an individual modeling system (e.g., WRF-CMAQ and WRF-
99 CHIMERE) was evaluated by considering its online and offline versions and under
100 various computing configurations (Wong et al., 2012; Briant et al., 2017), the
101 computational efficiencies of multiple two-way coupled models need to be accessed
102 under the same computing conditions as well.

103 In this paper, a comparative evaluation of three open-sourced two-way coupled
104 meteorology and air quality models (WRF-CMAQ, WRF-Chem and WRF-CHIMERE)
105 in ECR is conducted. The remainder of the paper is organized as follows: Section 2
106 describes the study methods including model configurations and evaluation protocols.
107 Sections 3 and 4 presents the analyses and intercomparisons of simulations from these
108 three two-way coupled models with regard to meteorology and air quality, respectively.
109 The major findings of this work are summarized in Section 5.

110

111 2 Data and methods

112 2.1 Model configurations and data sources

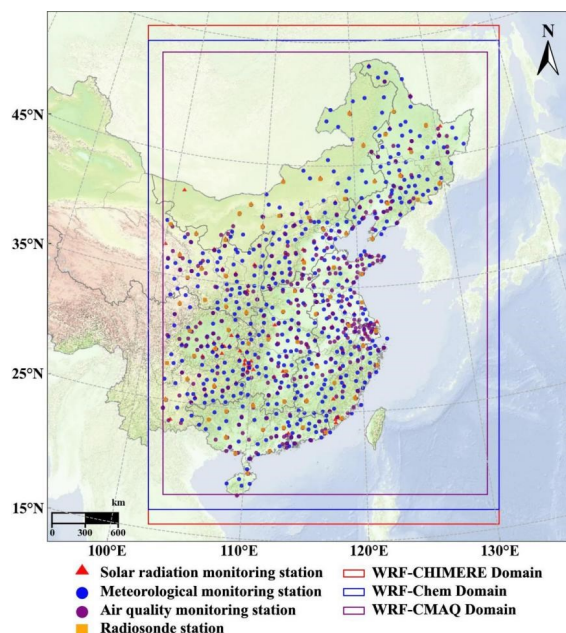
113 One-year long-term simulations in eastern China were examined using the two-
114 way coupled WRF v4.1.1-CMAQ v5.3.1, WRF-Chem v4.1.1, and WRF v3.7.1-
115 CHIMERE v2020r1 models, with and without enabling ARI and/or ACI, and with 27-
116 km horizontal grid spacing (there were 110, 120, and 120 grid cells in the east–west
117 direction, and 150, 160, and 170 in the north–south direction for WRF-CMAQ, WRF-
118 Chem, and WRF-CHIMERE, respectively). The vertical resolution for all simulations
119 consisted of 30 levels from the surface (~20 m) to 100 hPa. The anthropogenic
120 emissions of Multi-resolution Emission Inventory for China (MEIC) (Li et al., 2017)
121 and FINN v1.5 biomass burning emissions were applied in our simulations, and their
122 spatial, temporal, and species allocations were performed using Python language.
123 Biogenic emissions were calculated using the Model of Emissions of Gases and
124 Aerosols from Nature version 3.0 (MEGAN v3.0) (Gao et al., 2019). Dust and sea-salt
125 emissions were both used with calculations of inline modules, as shown in Table 1. The
126 meteorological ICs and BCs were derived from the National Center for Environmental
127 Prediction Final Analysis (NCEP-FNL) datasets (<http://rda.ucar.edu/datasets/ds083.2>),
128 with a horizontal resolution of $1^\circ \times 1^\circ$ at 6-hour intervals for each of the three coupled
129 models. To improve the long-term accuracy of meteorological variables when using the
130 WRF model, options of observational and grid four-dimensional data assimilation
131 (FDDA) were turned on, and pressure, station height, relative humidity, wind speed,



132 and wind direction were observed four times per day at 00:00, 06:00, 12:00, and 18:00
133 UTC from 2168 stations (<https://doi.org/10.5281/zenodo.6975602>). The chemical
134 ICs/BCs were downscaled from the Whole Atmosphere Community Climate Model
135 (WACCM) for WRF-CMAQ and WRF-Chem via the `mozart2camx` and `mozbc` tools,
136 respectively. The options of parameterization schemes of aerosol–radiation–cloud
137 interactions are summarized in Table 1. It should be noted that ACI processes cannot be
138 implemented in the official release of WRF-CMAQ.

139 To demonstrate the capabilities of the three two-way coupled models with/without
140 feedbacks in simulating meteorology and air quality, we undertook comprehensive
141 evaluations of the strengths and weaknesses each coupled model, validated against
142 extensive ground-based and satellite measurements. Ground-based data included 572
143 hourly ground-based meteorological observations (air temperature (T2) and relative
144 humidity (RH2) air temperature at 2m above the surface, wind speed at 10m above the
145 surface (WS10), and precipitation (PREC)) (<http://data.cma.cn>), 327 hourly national
146 environmental observations (fine particulate matter (PM_{2.5}), ozone (O₃), nitrogen
147 dioxide (NO₂), sulfur dioxide (SO₂), and carbon monoxide (CO))
148 (<http://106.37.208.233:20035>), 109 hourly surface shortwave radiation (SSR)
149 measurements (Tang et al., 2019) and 74 radiosonde sites retrieved twice per day (Guo
150 et al., 2019); the locations of these data are depicted in Figure 1. Because there were no
151 observed water vapor mixing ratio (w) data, this parameter was calculated via the
152 formula $w = \frac{rh}{w_s}$, where rh is the relative humidity and w_s is the saturation mixing ratio
153 (Wallace and Hobbs, 2006).

154 Satellite data included the following: monthly average downwelling short-/long-
155 wave flux at the surface and short-/long-wave flux at the top of the atmosphere (TOA)
156 from the Clouds and the Earth's Radiant Energy System (CERES)
157 (<https://ceres.larc.nasa.gov>); precipitation from the Tropical Rainfall Measuring
158 Mission (TRMM); cloud fraction, liquid water path (LWP), and aerosol optical depth
159 (AOD) from the Moderate Resolution Imaging Spectroradiometer (MODIS);
160 tropospheric NO₂ column and SO₂ column in the planetary boundary layer (PBL) from
161 the Ozone Monitoring Instrument (OMI); total CO column from the Measurements of
162 Pollution in the Troposphere (MOPITT) (<https://giovanni.gsfc.nasa.gov/giovanni>);
163 total column ozone (TCO) from the Infrared Atmospheric Sounding Interferometer-
164 Meteorological Operational Satellite-A (IASI-METOP-A)
165 (<https://cds.climate.copernicus.eu/cdsapp#!/dataset/satellite-ozone?tab=form>); and
166 total ammonia (NH₃) column from IASI-METOP-B ([https://cds-
167
168
169
170](https://cds-espri.ipsl.fr/iasibl3/iasi_nh3/V3.1.0)



171
 172 Figure 1. Modeling domains (WRF-CMAQ, WRF-Chem, and WRF-CHIMERE), and solar
 173 radiation, meteorology, air quality, and radiosonde stations.

174 Table 1. Model configurations and parameterization schemes.

Configurations	WRF-CMAQ	WRF-Chem	WRF-CHIMERE
Horizontal grid spacing	27 km (110 × 150)	27 km (120 × 160)	27 km (120 × 170)
Vertical grid	30 levels	30 levels	30 levels
Shortwave radiation	RRTMG	RRTMG	RRTMG
Longwave radiation	RRTMG	RRTMG	RRTMG
Aerosol mixing state	Core-Shell	Core-Shell	Core-Shell
Cloud microphysics	Morrison	Morrison	Thompson
PBL	ACM2	YSU	YSU
Cumulus	Kain-Fritsch	Grell-Freitas	Grell-Freitas
Surface	Pleim-Xiu	Monin-Obukhov	Monin-Obukhov
Land surface	Pleim-Xiu LSM	Noah LSM	Noah LSM
Gas-phase chemistry	CB6	CBMZ	MELCHIOR2
Photolysis	Fast-JX	Fast-JX	Fast-JX
Aerosol mechanism	AERO6	MOSAIC 4BIN	SAM 10BIN
Anthropogenic emission	MEIC 2017	MEIC 2017	MEIC 2017
Biogenic emission	MEGAN v3.0	MEGAN v3.0	MEGAN v3.0
Biomass burning emission	FINN v1.5	FINN v1.5	FINN v1.5
Dust emission	Foroutan	GOCART	Menuet
Sea-salt emission	Gong	Gong	Monahan
Meteorological ICs and BCs	FNL	FNL	FNL
Chemical ICs and BCs	MOZART	MOZART	LMDZ-INCA



175 2.2 Scenario set up

176 Eight sets of hindcast WRF-CMAQ, WRF-Chem, and WRF-CHIMERE
 177 simulations with/without aerosol feedbacks were carried out to investigate the
 178 performance of each coupled model over eastern China during 2017, as presented in
 179 Table 2. It should be noted that the officially released WRF-Chem and WRF-CHIMERE
 180 are capable of simulating ARI and ACI, but WRF-CMAQ is not. In all of the
 181 simulations performed in this study, a month of spin-up time was set up to reduce the
 182 influence of the initial conditions. We calculated multiple model evaluation metrics
 183 between each scenario simulation and relevant observations to assess the model
 184 performance; these included the correlation coefficient (R), mean bias (MB),
 185 normalized mean bias (NMB), and root mean square error (RMSE). The mathematical
 186 definitions of these metrics are provided in Supplement S1. We comprehensively
 187 analyzed the annual and seasonal statistical metrics of meteorological and air quality
 188 variables including simulations by all three two-way coupled models with/without
 189 enabling ARI and/or ACI effects. We then quantified the respective contributions of the
 190 ARI and ACI effects to model performance.
 191

192 Table 2. Summary of scenarios setting in three coupled models.

Model	Scenario	Configuration option	Description
WRF-CMAQ	(1) WRF-CMAQ_NO	DO_SW_CAL=F	Without aerosol feedbacks
	(2) WRF-CMAQ_ARI	DO_SW_CAL=T	ARI
WRF-Chem	(3) WRF-Chem_NO	aer_ra_feedback=0 wetscav_onoff=0 cldchem_onoff=0	Without aerosol feedbacks
	(4) WRF-Chem_ARI	aer_ra_feedback=1 wetscav_onoff=0 cldchem_onoff=0	ARI
	(5) WRF-Chem_BOTH	aer_ra_feedback=1 wetscav_onoff=1 cldchem_onoff=1	ARI and ACI
WRF-CHIMERE	(6) WRF-CHIMERE_NO	direct_feed_chimere=0 indirect_feed_chimere=0	Without aerosol feedbacks
	(7) WRF-CHIMERE_ARI	direct_feed_chimere=1 indirect_feed_chimere=0	ARI
	(8) WRF-CHIMERE_BOTH	direct_feed_chimere=1 indirect_feed_chimere=1	ARI and ACI

193

194 3 Meteorological evaluations and intercomparisons

195 This section presents annual and seasonal (March–April–May, Spring; June–July–
 196 August, Summer; September–October–November, Autumn; and December–January–
 197 February, Winter) statistical metrics of simulated meteorological variables and air
 198 quality when compared with ground-based and satellite observations, as well as a



199 discussion of the running times of the eight scenario simulations.

200 3.1 Ground-based observations

201 Figures 2 and S1–S7 illustrate comparisons of the spatial distributions of R, MB,
202 and RMSE for hourly SSR, T2, Q2, RH2, WS10, PREC, PBLH00, and PBLH12 from
203 WRF-CMAQ, WRF-Chem, and WRF-CHIMERE with/without turning on aerosol
204 feedbacks against ground-based observations from each site across the whole of 2017.
205 The calculated annual model evaluation metrics for all sites in eastern China are
206 summarized in Table S1, and the related seasonal R and MB values are presented in
207 Figure 3.

208 The accuracy of radiation predication is of great significance in evaluating ARI.
209 Yearly and seasonal average simulated SSR data were explicitly compared with ground-
210 based observations (Figure 3 and Table S1); the SSR over eastern China was simulated
211 reasonably well by all models with R values in the range of 0.61–0.78. The overall
212 model performances of WRF-CMAQ and WRF-Chem were better than that of WRF-
213 CHIMERE, while all simulated results were overestimated at both annual and seasonal
214 scales (MBs in spring and summer were larger than those in autumn and winter). The
215 overestimations of annual SSR were 19.98, 14.48, and 9.24 W m⁻² for WRF-CMAQ,
216 WRF-Chem, and WRF-CHIMERE, respectively. Overestimations of SSR by most two-
217 way coupled models were also reported for Europe and North America in the
218 comparative study conducted by Brunner et al. (2015). Such overestimations could be
219 explained by multiple factors, namely, the uncertainties in cloud development owing to
220 PBL and convection parameterizations (Alapaty et al., 2012), and the diversity in
221 treatment of land surface processes (Brunner et al., 2015), which appear to play more
222 important roles than does the enabling of two-way aerosol feedbacks on SSR through
223 ARI and ACI effects in the models. When the three models considered ARI effects, they
224 effectively improved the simulation accuracy of SSR, over both the whole year and in
225 the four seasons, but the enabling of ACI effects resulted in relatively limited
226 improvement. In addition, the MB variations of WRF-CMAQ and WRF-Chem
227 simulations were higher in spring and winter than those in summer and autumn, while
228 the MB of WRF-CHIMERE simulations showed a maximum in summer (−10.33 W
229 m⁻²) and minimum in autumn (−7.64 W m⁻²). Both the annual and seasonal reductions
230 in SSR simulated by WRF-Chem and WRF-CHIMERE with ACI effects enabled were
231 much smaller than those with ARI effects enabled.

232 In general, the simulated magnitudes and temporal variations of air temperature
233 and water vapor mixing ratio at 2 m above the ground showed a high order of
234 consistency with observations (R = 0.88–0.97). Looking at annual and seasonal T2,
235 models tended to have a negative (cool) bias, and T2 underestimations in spring and
236 winter were greater than those in summer and autumn. As pointed out by Makar et al.
237 (2015a), WRF-CHEM and GEM-MACH gave negative MBs in summer and positive
238 MBs in winter when both ACI and ARI effects were enabled (BOTH), and WRF-
239 CMAQ with only ARI effects enabled also produced negative MBs in summer over
240 North America during 2010; note that the Makar et al (2015a) study lacked evaluations
241 of meteorology in winter using WRF-CMAQ. The comparison results of MBs indicated
242 that WRF-CHIMERE > WRF-CMAQ > WRF-Chem. The annual and seasonal MBs of



243 WRF-CMAQ and WRF-Chem were approximately -1 °C, while those of WRF-
244 CHIMERE ranged from -2 to -1 °C. The RMSEs were approximately equal for WRF-
245 CMAQ (2.71 – 3.05 °C) and WRF-Chem (2.82 – 3.27 °C), and larger for WRF-
246 CHIMERE (3.39 – 4.53 °C), at both annual and seasonal scales. It is noteworthy that
247 underestimations of annual and seasonal T2 were mitigated in eastern China in the three
248 coupled models when ARI effects were enabled. When ACI effects were enabled, the
249 MBs for T2 simulated by WRF-Chem_BOTH showed no significant changes compared
250 with those of WRF-Chem_NO; WRF-CHIMERE_BOTH further enhanced the
251 underestimations of T2 in the full year (-1.30 °C), spring (-0.12 °C), and winter
252 (-0.40 °C) compared with WRF-CHIMERE_NO.

253 For Q2, WRF-CMAQ showed the best performance, followed by WRF-Chem, and
254 WRF-CHIMERE (Table S1 and Figure S2), all with RMSEs of less than 3 g kg⁻¹. Most
255 models tended to underestimate annual and seasonal Q2 (-0.57 to -0.18 g kg⁻¹ and
256 -1.16 to $+0.20$ g kg⁻¹, respectively), and the underestimations were most significant in
257 summer. However, multiple two-way coupled models produced slightly positive values
258 for Q2 during January 2010 over the North China Plain in the MICS-Asia III project
259 (Gao et al., 2018). Compared with simulations that did not have aerosol feedbacks
260 enabled, WRF-CMAQ_ARI and WRF-CHIMERE_ARI increased the negative biases
261 of annual and seasonal Q2, with the former being more significant (Figure 3 and Table
262 S1). The changes in annual, summer, and autumn MBs for WRF-Chem_ARI were
263 consistent with the trend of WRF-CMAQ_ARI, except for spring and winter.

264 Looking at RH2, annual and seasonal simulations using WRF-CMAQ had the
265 highest correlation with the observed values, followed by WRF-Chem, and WRF-
266 CHIMERE, and the smallest correlation coefficients for all three models occurred in
267 autumn (~ 0.5). The spatial MBs between simulations by the three models and
268 observations showed a general converse trend compared with T2 (i.e., RH2 was
269 overestimated where T2 was underestimated, and vice versa). This can be explained by
270 the calculation of RH2 being based on T2 in the models (Wang et al., 2021). The annual
271 and seasonal MBs were approximately 0.65% – 71.03% and -21.30% to 60.00% ,
272 respectively (Figure 3 and Table S1), and only WRF-Chem produced negative MBs in
273 summer. The magnitude of RMSE showed an inverse pattern compared with R for all
274 three models, with maximum (28.48% – 29.52%) and minimum (12.57% – 16.07%)
275 values shown in autumn and summer, respectively. As shown in Figure 3 and Table S1,
276 WRF-CMAQ_ARI further reduced the overestimations of annual and seasonal RH2 in
277 eastern China, while WRF-Chem_ARI (except for summer) and WRF-CHIMERE_ARI
278 showed the opposite trend. Moreover, variations in annual and seasonal RH2 MBs
279 simulated by WRF-Chem_BOTH and WRF-CHIMERE_BOTH were further reduced
280 compared with WRF-Chem_ARI (except for summer) and WRF-CHIMERE_ARI,
281 respectively.

282 Similar analyses were also performed for WS10, and revealed that WRF-CMAQ
283 performed better in capturing WS10 patterns compared with WRF-Chem and WRF-
284 CHIMERE. The R values for all three models ranged from 0.47 to 0.60 ; WRF-CMAQ
285 and WRF-Chem overestimated wind speed by approximately 0.5 m s⁻¹, while WRF-
286 CHIMERE overestimated it by approximately 1.0 m s⁻¹. The overestimation of WS10



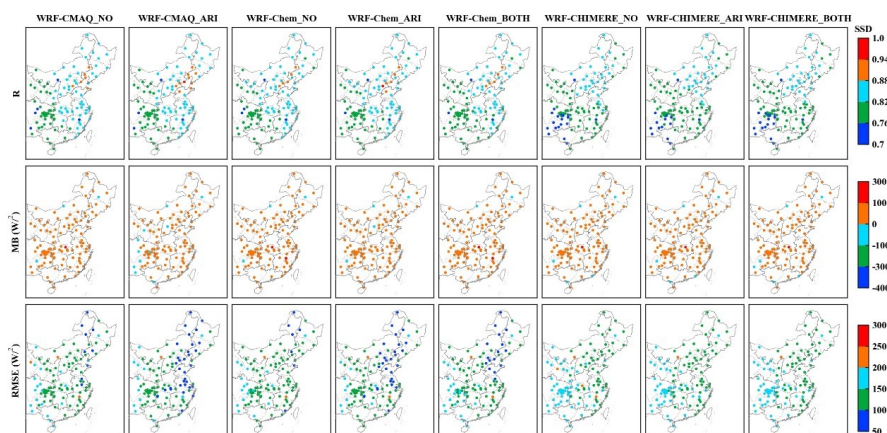
287 under real-world low wind conditions is a common phenomenon of current weather
288 models, which is mainly caused by outdated geographic data, coarse model resolution,
289 and a lack of a good physical representation of the urban canopy (Gao et al., 2015; Gao
290 et al., 2018). All three models presented lower correlations (0.31–0.54) and MBs (0.20–
291 0.86 m s⁻¹) in summer compared with other seasons, and the RMSEs were
292 approximately 2.0 m s⁻¹. When ARI effects were enabled, the overestimations of the
293 three models were alleviated, especially for WRF-CMAQ_ARI.

294 The annual and seasonal correlation coefficients of precipitation were 0.56–0.69,
295 0.46–0.63, and 0.25–0.55 for WRF-CMAQ, WRF-Chem, and WRF-CHIMERE,
296 respectively (Table S1 and Figure S5). All simulated results had the highest correlations
297 in winter and the lowest in summer, because the convective activity was enhanced in
298 summer and the models struggle to effectively capture this. WRF-CMAQ and WRF-
299 CHIMERE (WRF-Chem except for autumn) underestimated and overestimated annual
300 and seasonal precipitation, respectively. At the annual and seasonal scales, WRF-Chem
301 and WRF-CHIMERE overestimated the magnitude of daily precipitation by more than
302 1 mm day⁻¹, while WRF-CMAQ underestimated it by approximately 0.5 mm day⁻¹. A
303 similar picture emerged for North America during 2010, whereby the magnitude of
304 precipitation MBs was higher in WRF-Chem than in WRF-CMAQ (see figure 11 in
305 Makar et al., 2015a). The largest precipitation MBs simulated by the three models
306 occurred in summer and ranged from –0.70 to +1.39 mm day⁻¹. The RMSE was highest
307 in WRF-CHIMERE, followed by WRF-Chem, and WRF-CMAQ, and all models had
308 the largest (> 10 mm day⁻¹) and smallest (approximately 2.5 mm day⁻¹) values in
309 summer and winter, respectively. When ARI effects were considered, WRF-
310 CMAQ_ARI simulations increased the annual and seasonal precipitation
311 underestimations in eastern China, while WRF-Chem_ARI (except for autumn) and
312 WRF-CHIMERE_ARI simulations reduced the precipitation overestimations. The
313 effects of ARI on summer MBs using all three coupled models were significant
314 compared with other seasons. When ACI effects were further included, WRF-
315 Chem_BOTH showed very limited improvement in the overestimation of precipitation
316 compared with WRF-Chem_NO, while WRF-CHIMERE_BOTH enhanced the
317 overestimation of precipitation, especially in summer.

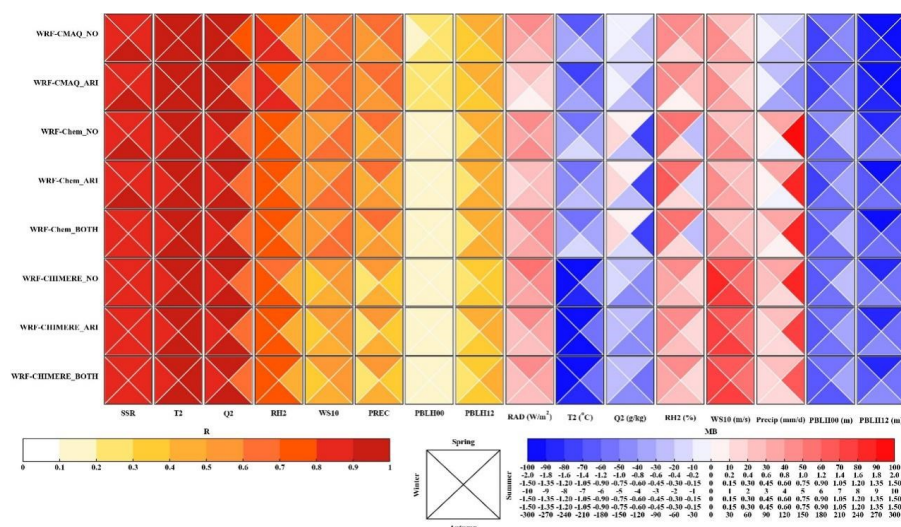
318 Overall, PBLH data were not well reproduced by any of the three coupled models,
319 which may be a result of the low resolution of the sounding data (Brunner et al., 2015)
320 and the different settings of Richardson number thresholds in calculating PBLH (Guo
321 et al., 2016). At 8:00 and 20:00 local time (LT), annual and seasonal PBLH simulated
322 by WRF-CMAQ had the highest correlations (R = 0.21–0.40) and largest negative MBs
323 (ranging from –400 to –133 m). The poor performance was mainly caused by: 1)
324 different configurations of the PBL scheme in this study, namely, WRF-CMAQ adopted
325 the ACM2 scheme with hybrid local–nonlocal closure, while WRF-Chem and WRF-
326 CHIMERE adopted the YSU scheme with non-local closure (Table 1); 2) the settings
327 of the Richardson number threshold varied owing to the unstable atmospheric
328 conditions, i.e., the YSU and ACM2 schemes used thresholds of 0 and 0.25,
329 respectively (Xie et al., 2012); 3) the entrainment layer was further considered in the
330 ACM2 scheme for PBLH calculations (Xie et al., 2012).



331 Meanwhile, all correlations of the three models at 20:00 LT ($R = 0.3\text{--}0.4$) were
332 better than those at 8:00 LT ($R = 0.1\text{--}0.2$), because the gradient of the rapid increase in
333 PBLH in the morning was larger than that of the gradual decrease in PBLH at night,
334 and hence more difficult to accurately simulate. In addition, the RMSEs of PBLH in
335 autumn (369.89–388.79 m) and winter (347.48–392.38 m) were smaller than those in
336 spring (405.61–622.37 m) and summer (348.80–570.16 m) for all three models. As
337 shown in Figure 3 and Table S1, the effects of aerosol feedbacks on MB and RMSE
338 were larger than that on R. Considering that the MBs of PBLH are important for the
339 simulation of air quality, the MBs were further analyzed here. For WRF-CMAQ, ARI
340 effects induced an increase (–1.93 m) and decrease (+6.66 m) in the annual
341 underestimations at 8:00 and 20:00 LT, respectively (Table S1). The negative MBs for
342 WRF-Chem_ARI and WRF-Chem_BOTH showed an increase (8:00 LT: –25.25 m,
343 20:00 LT: –25.60 m) and decrease (8:00 LT: +19.65 m, 20:00 LT: +14.09 m) compared
344 with those for WRF-Chem_NO and WRF-Chem_ARI, respectively. The ARI (–6.17
345 and –3.34 m) and ACI (–0.65 and –1.11 m) effects both further underestimated annual
346 PBLH at 8:00 and 20:00 LT for WRF-CHIMERE. The variations in MBs induced by
347 aerosol feedbacks for the three coupled models at the annual scale were similar to those
348 at the seasonal scale.
349



350
351 Figure 2. Statistical metrics (R, MB, and RMSE) between annual simulations and observations of
352 surface shortwave radiation in eastern China.
353



354

355 Figure 3. Portrait plots of statistical indices (R and MB) between seasonal simulations and surface
 356 observations of meteorological variables (SSR, T2, Q2, RH2, WS10, PREC, and PBLH) at LT 08:00
 357 and 20:00) in eastern China.

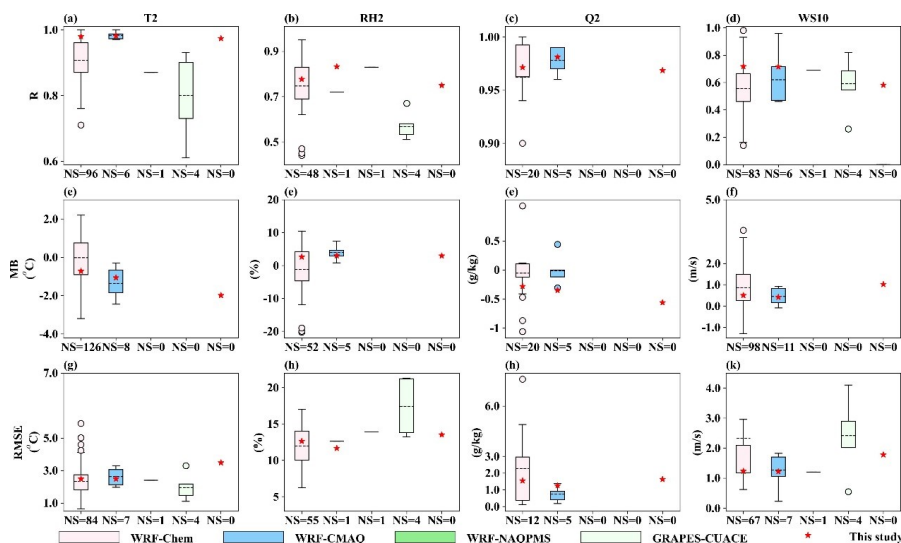
358

359 To identify and quantify how well our results compare with previous studies using
 360 two-way coupled models, we here discuss comparisons between our work and earlier
 361 research in terms of the evaluation results of meteorology and air quality; meteorology
 362 is discussed in this section and air quality is discussed in Section 4.1. Box-and-whisker
 363 plots were used and the 5th, 25th, 75th, and 95th percentiles were used as statistical
 364 indicators. In the plots, the dashed lines in the boxes are the mean values, and the circles
 365 represent outliers. Previous studies mainly used WRF-Chem and WRF-CMAQ to evaluate
 366 meteorology and air quality, while applications of WRF-NAQPMS and GRAPES-CUACE
 367 were scarce. As mentioned in Section 1, investigations of meteorology and air quality
 368 using WRF-CHIMERE with/without aerosol feedbacks have not previously been conducted
 369 in eastern China. Therefore, only evaluation results involving WRF-Chem and WRF-CMAQ
 370 to study aerosol feedbacks are analyzed herein.

371 Figure 4 illustrates the statistical metrics of T2, RH2, Q2, and WS10 in this study
 372 compared with the evaluation results of previous studies. According to the number of
 373 samples (NS) in the statistical metrics of each meteorological variable, most previous
 374 studies mainly involved the simulation and evaluation of T2, WS10, and RH2, with
 375 relatively few studies focusing on Q2. Compared with the evaluation results of previous
 376 studies, the ranges of statistical metrics in our study were roughly similar, but there
 377 were some important differences. The R values of the WRF-CMAQ and WRF-Chem
 378 models in our study were higher than those of previous studies; the MBs of T2 simulated
 379 via WRF-CMAQ were smaller, but those of T2 simulated via WRF-Chem were larger;
 380 and the RMSEs of the WRF-CMAQ simulation were larger, but those of the WRF-
 381 Chem simulation were smaller. For RH2, the R values for WRF-CMAQ and WRF-
 382 Chem in this study were all larger than the average level of previous studies, while the



383 MBs and RMSEs for WRF-CMAQ were larger, and those for WRF-Chem were smaller
 384 than the average of previous studies. For Q2, the model performance of WRF-CMAQ
 385 in this study was generally better than the average level of previous studies, but the R
 386 between WRF-Chem simulation results and observed values was higher (and MB and
 387 RMSE were lower) than the average level of previous studies. We also conclude that
 388 the simulation results of WRF-CMAQ and WRF-Chem in our study better reproduced
 389 variations in WS10 compared with previous studies (Fig. 4d).
 390



391
 392 Figure 4. Comparisons of model capacities between our study (red stars) and previous literature
 393 (box plots) in terms of the surface T2, RH2, Q2, and WS10 in eastern China. Note that red stars in
 394 the fifth column of each subgraph represent the statistical metrics of WRF-CHIMERE in this study.
 395

396 3.2 Satellite-borne observations

397 To further evaluate the wider spatial performance of WRF-CMAQ, WRF-Chem,
 398 and WRF-CHIMERE, we analyzed the annual and seasonal statistical metrics of short-
 399 and long-wave radiation at the surface and top of the atmosphere (TOA), precipitation,
 400 cloud cover, and liquid water path simulated by the three coupled models with and
 401 without aerosol feedbacks, via comparisons between simulations and satellite-borne
 402 observations (Table 3; Figures 5, S8–S13).

403 As listed in Table 3, the three coupled models predicted the longwave radiation
 404 variables at the surface (SLR) and top of the atmosphere (TLR) well (R values of 0.74
 405 to 0.99), with annual domain-average MBs of -9.97 to -6.05 W m^{-2} and -2.14 to 0.66
 406 W m^{-2} , respectively. The annual SLRs were underestimated by all three models, and
 407 the MBs of WRF-CMAQ (-6.46 to -6.05 W m^{-2}) were smaller than those of WRF-
 408 CHIMERE (-9.66 to -8.39 W m^{-2}) and WRF-Chem (-9.97 to -9.34 W m^{-2}). For
 409 annual TLR, the simulation results of WRF-CHIMERE (-0.96 to $+0.05$ W m^{-2}) and
 410 WRF-CMAQ (-2.14 to -1.42 W m^{-2}) provided underestimations, but WRF-Chem
 411 (0.28 – 0.71 W m^{-2}) gave overestimations. Significant seasonal differences in simulated



412 longwave radiation were also present among the three coupled models; all WRF-
413 CMAQ and WRF-CHIMERE scenarios gave underestimations, with maximum and
414 minimum values of SLR in winter and summer, respectively, while the maximum
415 underestimations of WRF-Chem occurred in autumn, especially for WRF-
416 Chem_BOTH (Figure S8). For seasonal TLR, the WRF-CMAQ and WRF-Chem model
417 performances were better than that of WRF-CHIMERE for all seasons except autumn
418 (Figure S9).

419 Compared with longwave radiation, the three coupled models showed poorer
420 performance for the shortwave radiation variables at the surface (SSR) and top of the
421 atmosphere (TSR) with annual MBs of 8.21–30.74 W m⁻² and -4.40 to +5.42 W m⁻²,
422 respectively, and correlations ranging from 0.61 to 0.92 for both variables. A similar
423 poor performance for shortwave radiation compared with longwave radiation was also
424 reported in the USA using the coupled WRF-CMAQ and offline WRF models (Wang
425 et al., 2021). The overall seasonal characteristics of SSR were successfully reproduced
426 by the three coupled models (Figure S10). Meanwhile, no matter whether aerosol
427 feedbacks were enabled or not, all three models overestimated seasonal SSR (except
428 for WRF-Chem_ARI in winter), and showed higher MBs in spring and summer than in
429 autumn and winter. The seasonal SSR overestimations may be a direct result of the
430 underestimation of calculated AOD when considering ARI effects (Wang et al., 2021).
431 Seasonal TSR was also successfully simulated by all three models, especially in winter
432 (Figure S11). No matter whether ARI and/or ACI effects were enabled or not, WRF-
433 CMAQ had negative MBs in all seasons, WRF-CHIMERE had negative MBs in all
434 seasons except for spring, and WRF-Chem produced underestimations and
435 overestimations of TSR in spring–summer and autumn–winter, respectively.

436 As all three coupled models adopted the same grid resolution (27 × 27 km) and
437 short- and long-wave radiation schemes (RRTMG), the above analysis demonstrates
438 that the configurations of different aerosol/gas chemical mechanisms contributed to the
439 diversity of seasonal MBs. Moreover, the three two-way coupled models with ARI
440 feedbacks enabled effectively improved the performances of annual and seasonal SSR;
441 however, for SLR, TLR, and TSR, performance improvements were much more
442 variable across the three coupled models and across different scenarios with and without
443 ARI and/or ACI feedbacks enabled. Further details on this can be found in Table S2.

444 From IPCC 2007 to IPCC 2021, the effects of aerosol feedbacks (especially for
445 ACI effects) on precipitation and cloud processes remain under debate. Here, we further
446 assessed annual and seasonal simulated precipitation, cloud cover, and liquid water
447 pathways in eastern China with high aerosol loadings against satellite observations
448 (Table 3 and Figures S11–S13), and attempted to provide new insights from a yearly
449 perspective into enabling online feedbacks in two-way coupled modeling simulations.

450 The results illustrated that correlations of precipitation via WRF-CMAQ (0.51–
451 0.89) were larger than those of WRF-Chem (0.61–0.73) and WRF-CHIMERE (0.54–
452 0.70). WRF-CMAQ had the best correlation in winter, while WRF-Chem and WRF-
453 CHIMERE had the best correlation in spring; all three models showed their worst
454 correlation in summer. The reason for this is that numerical models struggle to
455 effectively capture enhanced convective activity in summer. Huang and Gao (2018)



456 also pointed out that accurate representations of lateral boundaries are crucial in
457 improving precipitation simulations during summer over China. WRF-CMAQ
458 underestimated annual precipitation, with MBs of -76.49 to -51.93 mm, while WRF-
459 Chem and WRF-CHIMERE produced large precipitation overestimations ranging from
460 $+108.04$ to $+207.05$ mm (Table 3), especially in regions of southern China (Figure S11).
461 WRF-CMAQ also produced negative biases (-27.89 to $+42.08$ mm) of seasonal
462 precipitation, excluding WRF-CMAQ_ARI in winter. WRF-Chem and WRF-
463 CHIMERE only underestimated seasonal precipitation in autumn (-31.39 to -26.89
464 mm) and winter (-7.12 to -4.43 mm), respectively (Figure S11). The variations in
465 annual and seasonal MBs of precipitation were consistent with changes in cloud fraction
466 and LWP (Zhang et al., 2016), which will be discussed in more detail below.

467 When aerosol feedbacks were considered, the ARI-induced reductions in the
468 annual MBs of precipitation for WRF-CMAQ, WRF-Chem, and WRF-CHIMERE were
469 24.56, 12.11, and 4.70 mm, respectively. WRF-Chem_BOTH (24.9 mm) and WRF-
470 CHIMERE_BOTH (3.41 mm) enhanced the overestimation of annual precipitation
471 compared with WRF-Chem_ARI and WRF-CHIMERE_ARI, respectively. Significant
472 increases ($+53.15$ mm) and decreases (-6.3 to -3.41 mm) in MBs in winter and summer,
473 respectively, were produced by WRF-CMAQ and the other two models with ARI effects
474 enabled compared with no feedbacks. WRF-Chem and WRF-CHIMERE with both ARI
475 and ACI effects enabled led to larger enhancements of MBs ($+3.54$ to $+7.46$) at the
476 seasonal scale (Figure S11). It must be noted that the discrepancies in simulated
477 precipitation could mainly be attributed to the selection of different microphysics and
478 cumulus schemes in WRF-CMAQ (Morrison and Kain-Fritsch), WRF-Chem (Morrison
479 and Grell-Freitas), and WRF-CHIMERE (Thompson and Grell-Freitas).

480 Cloud fraction (CF) and LWP can significantly influence the spatiotemporal
481 distributions of precipitation; our simulated results of annual and seasonal CF over
482 eastern China are presented in Table 3 and Figure S12. Overall, WRF-CMAQ
483 performed best in simulating CF. The R values for WRF-Chem during summer (0.69)
484 and winter (0.70) were larger than those of WRF-CMAQ (0.59 and 0.64) and WRF-
485 CHIMERE (0.56 and 0.66), while WRF-CMAQ and WRF-CHIMERE showed better
486 simulation results in winter and autumn with correlations of up to 0.89 and 0.67,
487 respectively. All three coupled models underestimated annual and seasonal CF with
488 MBs that ranged from -16.83% to -6.18% and -21.13% to -4.13% , respectively; these
489 were consistent with previous two-way coupled modeling studies using WRF-CMAQ
490 (-19.7%) and WRF-Chem (-32% to -9%) in China (Hong et al., 2017; Zhao et al.,
491 2017).

492 All models reasonably simulated annual LWP in eastern China, with R values
493 above 0.55 and negative biases varying from -57.36 to -31.29 g m^{-2} . The
494 underestimations were closely related to missing cloud homogeneity (Wang et al., 2015;
495 Dionne et al., 2020) and excessive conversion of liquid to ice in all selected cloud
496 microphysics schemes (Klein et al., 2009). As shown in Figure S13, all models showed
497 their best performance in simulating LWP in spring ($R = 0.51$ – 0.79) and exhibited the
498 largest underestimations in winter (MBs of -54.82 to -40.89 g m^{-2}), except for WRF-
499 Chem, which had its maximum bias in autumn.



500 In terms of quantitatively determining the functions of aerosol feedbacks on CF
 501 and LWP, all simulated scenarios revealed that WRF-CMAQ_ARI overwhelmingly
 502 decreased annual and seasonal underestimations of CF (0.48%–1.05%) and LWP (3.03–
 503 4.29 g m⁻²), while there were slightly increased underestimations (CF: 0.02%–0.39%;
 504 LWP: 0.03–0.58 g m⁻²) in WRF-Chem_ARI and WRF-CHIMERE_ARI. Larger
 505 variations in annual and seasonal MBs of CF (0.23%–0.93%) and LWP (–2.96 g m⁻² to
 506 7.38 g m⁻²) were produced by WRF-CHIMERE_BOTH compared with WRF-
 507 CHIMERE_ARI. WRF-Chem_BOTH showed equivalent variations (CF: 0.03%–
 508 0.71%; LWP: 0.02–2.89 g m⁻²) to those of WRF-Chem_ARI. Although we have
 509 obtained preliminary quantitative results of the ACI effects on regional precipitation,
 510 CF, and LWP, it should be kept in mind that several limitations in representing ACI
 511 effects still exist in state-of-the-art two-way coupled models; these include a lack of
 512 consideration of the responses of convective clouds to ACI (Tuccella et al., 2019), and
 513 a lack of numerical descriptions of giant cloud condensation nuclei (Wang et al., 2021)
 514 and heterogeneous ice nuclei (Keita et al., 2020).

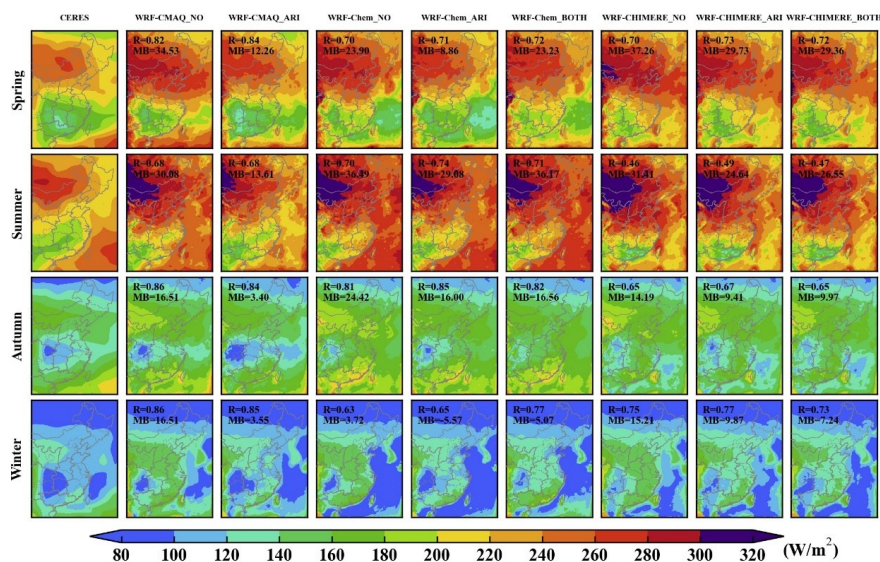
515
 516 Table 3. Statistical metrics (R, MB, NMB, and RMSE) between annual simulations and
 517 satellite retrievals of surface shortwave and longwave radiation, TOA shortwave and
 518 longwave radiation, precipitation, cloud fraction, and liquid water path in eastern China.
 519 The best results are in bold, while mean simulations and observations are in italics.

Variables	Statistics	WRF-CMAQ_NO	WRF-CMAQ_ARI	WRF-Chem_NO	WRF-Chem_ARI	WRF-Chem_BOTH	WRF-CHIMERE_NO	WRF-CHIMERE_ARI	WRF-CHIMERE_BOTH
Surface	Mean_sim	<i>197.15</i>	<i>180.94</i>	<i>203.48</i>	<i>194.52</i>	<i>201.45</i>	<i>197.39</i>	<i>191.34</i>	<i>195.58</i>
shortwave radiation (172.74 W m ⁻²)	R	0.76	0.75	0.73	0.78	0.75	0.61	0.64	0.66
	MB	24.41	8.21	30.74	21.78	28.71	24.75	18.71	22.94
	NMB (%)	14.13	4.75	17.79	12.61	16.62	14.34	10.84	13.29
	RMSE	30.25	20.37	35.34	26.88	32.80	34.70	29.60	31.45
Surface	Mean_sim	<i>316.25</i>	<i>315.83</i>	<i>312.96</i>	<i>312.60</i>	<i>312.32</i>	<i>313.33</i>	<i>314.60</i>	<i>314.47</i>
longwave radiation (322.3 W m ⁻²)	R	0.98	0.98	0.98	0.98	0.98	0.99	0.99	0.99
	MB	-6.05	-6.46	-9.34	-9.70	-9.97	-9.66	-8.39	-8.53
	NMB (%)	-1.88	-2.00	-2.90	-3.01	-3.09	-2.99	-2.60	-2.64
	RMSE	13.65	14.13	14.81	14.97	15.17	15.47	14.52	14.72
TOA	Mean_sim	<i>107.76</i>	<i>112.68</i>	<i>110.38</i>	<i>110.95</i>	<i>107.16</i>	<i>114.33</i>	<i>116.62</i>	<i>113.09</i>
shortwave radiation (111.56 W m ⁻²)	R	0.81	0.79	0.69	0.68	0.62	0.65	0.65	0.65
	MB	-3.80	1.13	-1.18	-0.61	-4.40	3.12	5.42	1.89
	NMB (%)	-3.40	1.01	-1.05	-0.55	-3.94	2.81	4.87	1.70
	RMSE	15.75	16.04	17.07	16.10	17.21	20.85	20.67	18.96
TOA	Mean_sim	<i>231.54</i>	<i>232.26</i>	<i>234.34</i>	<i>233.96</i>	<i>234.39</i>	<i>232.52</i>	<i>232.17</i>	<i>233.18</i>
longwave radiation (233.68 W m ⁻²)	R	0.88	0.90	0.91	0.91	0.92	0.74	0.74	0.76
	MB	-2.14	-1.42	0.66	0.28	0.71	-0.61	-0.96	0.05
	NMB (%)	-0.92	-0.61	0.28	0.12	0.30	-0.26	-0.41	0.02
	RMSE	6.94	6.20	6.00	5.94	5.86	10.10	10.07	9.70
Precipitation	Mean_sim	<i>872.42</i>	<i>896.98</i>	<i>1069.06</i>	<i>1056.95</i>	<i>1081.84</i>	<i>1165.06</i>	<i>1160.35</i>	<i>1163.77</i>
(948.91 mm y ⁻¹)	R	0.71	0.71	0.71	0.71	0.70	0.69	0.69	0.69
	MB	-76.49	-51.93	120.15	108.04	132.94	207.05	202.35	205.76



	NMB (%)	-9.23	-8.40	12.66	11.39	14.01	21.61	21.12	21.48
	RMSE	573.14	595.76	675.91	668.92	693.74	776.60	786.36	790.73
Cloud cover (64.09 %)	Mean_sim	52.51	53.32	48.18	47.80	47.46	58.12	57.98	58.55
	R	0.68	0.68	0.69	0.69	0.68	0.66	0.66	0.64
	MB	-11.58	-10.77	-16.12	-16.50	-16.83	-6.60	-6.74	-6.18
	NMB (%)	-18.07	-16.80	-25.07	-25.66	-26.18	-10.20	-10.41	-9.54
	RMSE	16.47	16.28	20.17	20.48	20.73	15.28	15.33	15.34
liquid water path (88.44 g m ⁻²)	Mean_sim	53.50	57.15	32.29	31.87	31.08	56.23	56.21	54.00
	R	0.61	0.58	0.47	0.46	0.28	0.55	0.55	0.51
	MB	-34.94	-31.29	-56.16	-56.58	-57.36	-32.37	-32.40	-34.61
	NMB (%)	-39.51	-35.38	-63.49	-63.97	-64.86	-36.54	-36.56	-39.06
	RMSE	54.35	54.31	63.54	63.92	67.21	53.39	53.42	55.86

520



521

522 Figure 5. Spatial distributions of seasonal SSR between CERES observations and
 523 simulations from WRF-CMAQ, WRF-Chem, and WRF-CHIMERE with and without
 524 aerosol feedbacks in eastern China.

525

526 4 Air quality evaluations and intercomparisons

527 In a similar way to meteorology, to further determine the quantitative effects of
 528 enabling aerosol feedbacks on the simulation accuracy of air quality variables in eastern
 529 China, ground-based and satellite-borne observations were adopted as comparisons in
 530 the following evaluation analysis. The usage status of computing resources during each
 531 simulation process is also assessed in Section 4.3.

532



533 4.1 Ground-based observations

534 Table 4 and Figure 6 present the statistical metrics of annual and seasonal air
535 pollutant concentrations ($PM_{2.5}$, O_3 , NO_2 , SO_2 , and CO) simulated by each of the three
536 coupled models. The R values of annual $PM_{2.5}$ concentrations for WRF-CMAQ (0.68)
537 were the highest, followed by WRF-Chem (0.65–0.68), and WRF-CHIMERE (0.52–
538 0.53). All three models showed higher correlations in winter compared with those in
539 other seasons (Figure 7). WRF-CMAQ underestimated annual and seasonal (except for
540 autumn) $PM_{2.5}$ concentrations with NMBs ranging from -9.78% to -6.39% and -17.68%
541 to $+5.17\%$, respectively. WRF-Chem generated both overestimations and
542 underestimations of $PM_{2.5}$ at the annual and seasonal scales, with related NMBs varying
543 from -39.11% to $+24.72\%$. Meanwhile, WRF-CHIMERE excessively overestimated
544 annual and seasonal $PM_{2.5}$ concentrations (NMB: $+19.51\%$ to $+75.47\%$). These biases
545 were produced by the configurations of different aerosol and gas phase mechanisms,
546 online dust emission schemes, and chemical ICs and BCs in the two-way coupled
547 models. Based on the differences in NMBs between simulations with ARI and those
548 with no aerosol feedbacks, ARI-induced annual and seasonal NMB variations of WRF-
549 CMAQ_ARI and WRF-Chem_ARI ranged from $+3.01\%$ to $+4.21\%$ and $+3.07\%$ to
550 $+5.02\%$, respectively, indicating that the enabling of ARI feedbacks slightly reduced
551 annual and seasonal (except for autumn) underestimations of $PM_{2.5}$ concentrations.
552 Note that WRF-CHIMERE_ARI further overestimated the annual and seasonal $PM_{2.5}$,
553 with an increase in NMB of up to 10.04% . The increases in $PM_{2.5}$ concentrations caused
554 by ARI effects can be attributed to synergetic decreases in SSR, T2, WS10, and PBLH,
555 and increases in RH2. With ACI feedbacks further enabled, WRF-Chem_BOTH largely
556 underestimated the annual and seasonal $PM_{2.5}$, with NMBs varying from -24.15% to
557 -14.44% compared with WRF-Chem_ARI. WRF-CHIMERE_BOTH tended to
558 decrease (-2.1% to -0.51%) annual and autumn–winter NMBs, and increase ($+0.35\%$
559 to $+3.04\%$) spring–summer NMBs. Further comparison between ARI- and ACI-
560 induced NMB variations demonstrates the key point that ARI-induced variations in
561 $PM_{2.5}$ concentrations were smaller than those induced by ACI in WRF-Chem, but this
562 pattern was reversed in WRF-CHIMERE. This may be explained by WRF-CHIMERE
563 incorporating the process of dust aerosols serving as IN, which was not included in
564 WRF-Chem in this study.

565 For O_3 , WRF-CHIMERE ($R = 0.62$) exhibited the best model performance,
566 followed by WRF-CMAQ ($R = 0.55$), and WRF-Chem ($R = 0.45$) (Table 4 and Figure
567 S15). WRF-CMAQ slightly underestimated annual O_3 , with NMBs of -7.83% to
568 -11.52% , but WRF-Chem and WRF-CHIMERE both significantly overestimated it,
569 with NMBs of 47.82% – 48.10% and 29.46% – 29.75% , respectively. The seasonal results
570 of statistical metrics showed patterns that were consistent with annual simulations, and
571 summer O_3 pollution levels were better simulated than those in other seasons (Figure
572 6). All models with ARI feedbacks enabled resulted in slight decreases in annual and
573 seasonal O_3 NMBs, ranging from -3.02% to $+0.85\%$ (the only positive value of $+0.85\%$
574 was produced by WRF-CMAQ in summer). Meanwhile, for ACI effects, WRF-Chem
575 and WRF-CHIMERE had increased annual O_3 NMBs of $+0.12\%$ and $+0.65\%$,
576 respectively. ACI-induced seasonal NMB variations were different for WRF-Chem



577 compared with WRF-CHIMERE; WRF-Chem increased in spring–summer and
578 decreased in autumn–winter, while WRF-CHIMERE increased in all seasons except for
579 winter (Figure 6). Such diversity in NMB variation can be explained by configuration
580 differences in gas-phase chemistry mechanisms, which involve various photolytic
581 reactions (a more detailed explanation can be found in Section 4.2).

582 A comprehensive assessment of the effects of seven gas-phase chemical
583 mechanisms (RADM2, RADMKA, RACM-ESRL, CB05Clx, CB05-TUCL, CBMZ,
584 and MOZART-4) on O₃ simulations via three two-way coupled models (WRF-Chem,
585 WRF-CMAQ, and COSMO-ART) was conducted by Knote et al. (2015); they
586 concluded that the O₃ concentrations simulated via WRF-Chem with the CBMZ
587 mechanism were closest to the mean values of multiple models over North America and
588 Europe in spring and summer. However, in contrast to North America and Europe, the
589 two-way coupled WRF-Chem with CBMZ had the poorest performance during spring
590 in eastern China. In addition, ARI and/or ACI effects contribute to atmospheric
591 dynamics and stability (as mentioned in the PBLH evaluation part of Section 3.1), as
592 well as photochemistry and heterogeneous reactions, and, in turn, they will eventually
593 influence O₃ formation (Xing et al., 2017; Qu et al., 2021; Zhu et al., 2021).

594 According to the annual statistical results (Table 4 and Figure S16), the NO₂
595 simulated by all three models had comparable correlations (0.50–0.60) with ground-
596 based observations. WRF-CMAQ slightly overestimated NO₂ (MBs of +2.74 to +3.26
597 μg m⁻³, and NMBs of +8.77% to +10.44%), but WRF-Chem (MBs of -10.03 to -9.22
598 μg m⁻³, and NMBs of -32.14% to -29.55%) and WRF-CHIMERE (MBs of -9.35 to
599 -8.96 μg m⁻³, and NMBs of -29.96% to -28.73%) tended to largely underestimate NO₂
600 in eastern China. For seasonal variations (Figure 6), WRF-CMAQ had the best
601 performance in winter, and generally overestimated NO₂ in all seasons (NMBs of -2.21%
602 to 34.34%). Both WRF-Chem and WRF-CHIMERE had maximum R and NMB values
603 (0.42–0.50 and -13.09% to -3.23%, respectively) in winter, and minimum values
604 (0.57–0.62 and -41.57% to -38.05%, respectively) in summer. The annual and seasonal
605 positive biases of WRF-CMAQ are partially caused by not incorporating the
606 heterogeneous reactions of NO₂ on ground and aerosol surfaces (Spataro et al., 2013;
607 Li et al., 2018; Liu et al., 2019). These gaps had been filled by Zhang et al. (2021) in
608 CMAQ v5.3 but not incorporated into the official released versions. For WRF-Chem
609 and WRF-CHIMERE, underestimations of NO₂ were consistent with overestimations
610 of O₃, because NO_x depletions were dominated by O₃ titrations. In addition, subtle
611 differences existed in the default settings of reaction rate constants for specific chemical
612 reactions in WRF-CMAQ, WRF-Chem, and WRF-CHIMERE; more detailed
613 information can be found in the source code files of mech_cb6r3_ae6_aq.def,
614 module_cbmz.F, and rates.F, respectively. With ARI feedbacks enabled, the annual and
615 seasonal R values of NO₂ simulated by WRF-CMAQ improved, but the NMB got worse;
616 both WRF-Chem and WRF-CHIMERE were improved. Our results show that ARI
617 effects tended to enhance NO₂ overestimations in WRF-CMAQ, and mitigate
618 underestimations in WRF-Chem and WRF-CHIMERE. This can be explained by the
619 ARI-induced NO₂ reductions being attributed to slower photochemical reactions, and
620 strengthened atmospheric stability and O₃ titration, and vice versa. When ACI effects



621 were further enabled in WRF-Chem and WRF-CHIMERE, the improvements in model
 622 performances were relatively limited.

623 All models performed most poorly for annual and seasonal SO₂ and CO
 624 simulations over eastern China (Table 4 and Figure 6). For SO₂, annual correlations
 625 were equivalent for all models, and ranged from 0.39 to 0.41. All three models
 626 underestimated SO₂; WRF-CMAQ showed the smallest MB (−4.31 μg m^{−3}), and WRF-
 627 Chem the largest (−10.30 μg m^{−3}). Gao et al. (2018) also showed that all two-way
 628 coupled models, except the WRF-Chem version from the University of Iowa modeling
 629 group, tended to underestimate SO₂ (−54.77 to 4.50 μg m^{−3}) over the North China Plain
 630 during January, 2013. The R values for all models were highest in autumn and winter
 631 (0.31–0.46), and lowest in spring and summer (0.16–0.38), but NMBs showed the
 632 opposite trend. As concluded by Liu et al. (2010), larger underestimations of seasonal
 633 SO₂ concentrations were caused by the weaker solar radiation and lesser amount of
 634 precipitation in winter compared with summer, which slowed down the photochemical
 635 conversion of SO₂ to SO₄^{2−}, wet scavenging, and aqueous-phase oxidation rates of SO₂.

636 For CO (Table 4), WRF-CHIMERE (0.47–0.48) had higher correlation
 637 coefficients than those of WRF-CMAQ (0.23–0.24) and WRF-Chem (0.21–0.22). All
 638 three models underestimated CO concentrations, with MBs ranging from −0.52 to
 639 −0.39 mg m^{−3}. These underestimations were partly caused by uncertainties in the
 640 vertical allocation of CO emissions (He et al., 2017). WRF-CMAQ and WRF-Chem
 641 both produced spring-minimum (0.15) and winter-maximum (0.36) seasonal cycles of
 642 R values (Figure 6), while WRF-CHIMERE had high (0.47) and low (0.26) correlations
 643 in winter and summer, respectively. Negative seasonal NMBs (−56.94% to −33.18%)
 644 were present in all coupled models. When ARI effects were considered, annual and
 645 seasonal SO₂ and CO model performances in all three models were slightly improved
 646 (R increased by approximately 0.01, and NMB increased by 0.98%–1.71%). Moreover,
 647 improvements in the simulation accuracies of SO₂ and CO for two-way coupled WRF-
 648 Chem and WRF-CHIMERE were dominated by ARI effects rather than ACI effects.

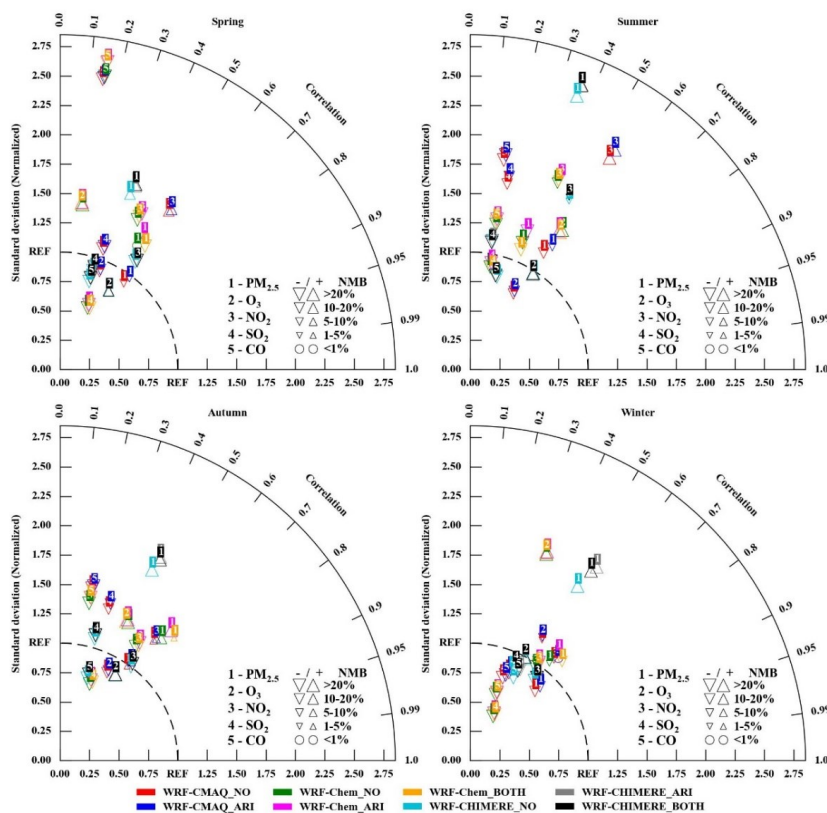
649
 650 Table 4. Statistical metrics (R, MB, NMB, and RMSE) between annual simulations and
 651 observations of surface PM_{2.5}, O₃, NO₂, SO₂, and CO in eastern China. The best results
 652 are in bold, while mean simulations and observations are in italics.

Variables	Statistics	WRF-CMAQ_NO	WRF-CMAQ_ARI	WRF-Chem_NO	WRF-Chem_ARI	WRF-Chem_BOTH	WRF-CHIMERE_NO	WRF-CHIMERE_ARI	WRF-CHIMERE_BOTH
PM _{2.5} (44.99 μg/m ³)	Mean_sim	<i>40.59</i>	<i>42.12</i>	<i>44.45</i>	<i>46.65</i>	<i>38.33</i>	<i>62.17</i>	<i>65.36</i>	<i>65.13</i>
	R	0.68	0.68	0.65	0.65	0.69	0.52	0.53	0.53
	MB	−4.40	−2.87	−0.54	1.66	−6.66	17.18	20.37	20.14
	NMB (%)	−9.78	−6.39	−1.21	3.69	−14.81	38.19	45.27	44.76
	RMSE	27.62	27.69	32.58	34.64	32.48	55.13	60.25	59.41
O ₃ (62.23 μg/m ³)	Mean_sim	<i>55.06</i>	<i>54.41</i>	<i>88.53</i>	<i>87.81</i>	<i>87.89</i>	<i>76.92</i>	<i>76.48</i>	<i>76.89</i>
	R	0.54	0.55	0.46	0.45	0.45	0.62	0.62	0.62
	MB	−7.17	−7.83	26.30	25.58	25.65	14.69	14.25	14.66
	NMB (%)	−11.52	−12.57	42.26	41.10	41.22	23.60	22.90	23.55
NO ₂	Mean_sim	<i>33.94</i>	<i>34.46</i>	<i>21.17</i>	<i>21.98</i>	<i>21.40</i>	<i>21.85</i>	<i>22.20</i>	<i>22.24</i>



(31.2 μg/m ³)	R	0.59	0.60	0.50	0.50	0.50	0.55	0.56	0.56
	MB	2.74	3.26	-10.03	-9.22	-9.80	-9.35	-9.00	-8.96
	NMB (%)	8.77	10.44	-32.14	-29.55	-31.40	-29.96	-28.84	-28.73
	RMSE	19.14	19.48	21.23	21.21	21.21	18.72	18.68	18.70
	Mean_sim	<i>14.02</i>	<i>14.39</i>	8.22	8.56	7.85	8.88	9.18	9.19
(18.51 μg/m ³)	R	0.40	0.40	0.44	0.44	0.46	0.40	0.41	0.41
	MB	-4.49	-4.12	-10.29	-9.95	-10.66	-9.63	-9.33	-9.32
	NMB (%)	-24.25	-22.24	-55.61	-53.76	-57.57	-52.02	-50.39	-50.34
	RMSE	21.11	21.30	20.13	20.02	20.20	22.07	22.17	22.18
	Mean_sim	<i>0.44</i>	<i>0.45</i>	0.53	0.54	0.53	0.56	0.58	0.57
(0.96 mg/m ³)	R	0.23	0.24	0.21	0.22	0.22	0.47	0.48	0.47
	MB	-0.52	-0.51	-0.43	-0.42	-0.43	-0.40	-0.39	-0.39
	NMB (%)	-53.97	-52.99	-45.10	-43.94	-44.68	-41.82	-40.11	-40.28
	RMSE	0.90	0.90	0.82	0.83	0.83	0.62	0.62	0.62

653

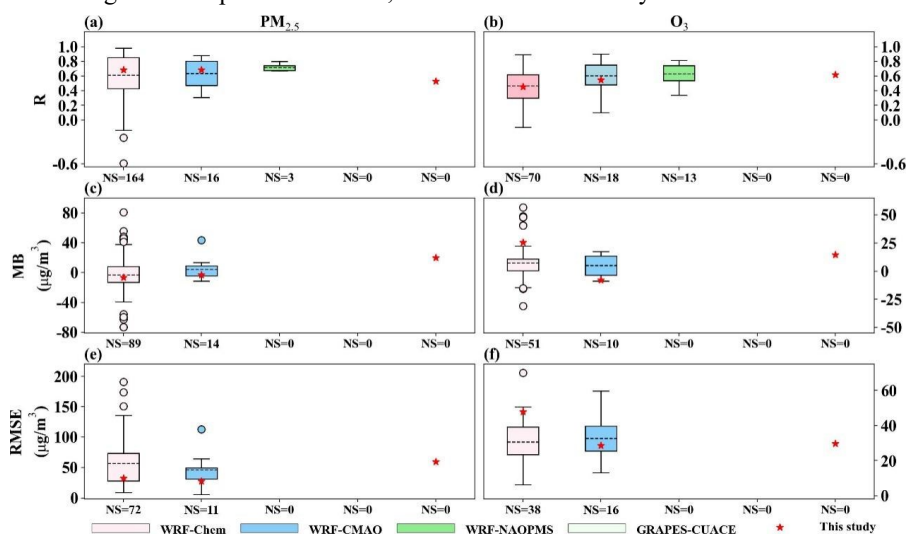


654

655 Figure 6. Taylor diagrams (R, normalized standard deviation, and NMB) of seasonal
 656 PM_{2.5}, O₃, NO₂, SO₂, and CO via three two-way coupled models (WRF-CMAQ, WRF-
 657 Chem, and WRF-CHIMERE) with/without ARI and/or ACI effects in eastern China
 658 compared with surface observations.



659 In a similar manner to the meteorological variables presented above, we aimed to
 660 conduct quality assurance for the statistical metrics by making further comparisons with
 661 PM_{2.5} and O₃ results from previous model evaluations (summarized in Figure 7). The
 662 performances of WRF-CMAQ and WRF-Chem in simulating PM_{2.5} in this study were
 663 better than the average levels of previous studies from eastern China. For O₃, WRF-
 664 Chem simulations performed worse than the average level of previous studies.
 665 Although the R values of O₃ simulated by WRF-CMAQ in this study were lower than
 666 the average level of previous studies, the RMSEs in this study were smaller.



667
 668 Figure 7. Comparisons of model capacities between our study (red stars) and previous literature
 669 (box plots) in terms of surface PM_{2.5} and O₃ concentrations in eastern China. Note that red stars in
 670 the fifth column of each subgraph represent the statistical metrics of WRF-CHIMERE in this study.
 671

672 4.2 Satellite-borne observations

673 In this section, we further investigate the discrepancies among different models in
 674 terms of the calculated AOD and column concentrations of gases (O₃, NO₂, SO₂, CO,
 675 and NH₃), and compare them with various satellite observations. For NH₃, owing to not
 676 setting the output of simulated NH₃ concentrations in WRF-CHIMERE, the discussion
 677 here only includes the results from WRF-CMAQ and WRF-Chem.

678 As shown in Table 5, annual AOD at 550 nm, TCO, NO₂, and CO simulated by all
 679 three models agreed most closely with satellite observations, with correlation
 680 coefficients of 0.80–0.98; these were followed by NH₃ (0.75–0.76), and SO₂ (0.50–
 681 0.53). WRF-CMAQ presented negative biases for annual AOD (−0.01), TCO (−5.92
 682 Dobson Units (DU)), SO₂ (−0.03 to −0.02 DU), CO (−1.25 × 10¹⁷ molecules cm^{−2}), and
 683 NH₃ (−2.95 × 10¹⁵ molecules cm^{−2}), but a positive bias for NO₂ (1.09–1.21
 684 petamolecules cm^{−2}). For AOD, WRF-Chem and WRF-CHIMERE produced positive
 685 and negative MBs of +0.09 and −0.06, respectively. Both WRF-Chem and WRF-
 686 CHIMERE overestimated NO₂ (0.28–0.63 petamolecules cm^{−2}) and CO (0.93–1.21 ×
 687 10¹⁷ molecules cm^{−2}), and underestimated O₃ (−10.99 to −3.63 DU) and SO₂ (−0.03 to



688 0.02 DU). Similar to WRF-CMAQ, WRF-Chem also underestimated NH_3 by
689 approximately -3.14×10^{15} molecules cm^{-2} .

690 For seasonal variations, relatively high correlation relationships (0.71–0.88) of
691 AOD were present in autumn, with lower values (0.53–0.84) in other seasons (Figure
692 9). WRF-CMAQ and WRF-Chem tended to underestimate AOD in summer (MBs of
693 -0.1 to -0.4) and overestimate it in other seasons (MBs of 0.01–0.05). WRF-
694 CHIMERE had positive biases (0.03–0.04) in winter and negative biases (-0.10 to
695 -0.01) in other seasons.

696 For TCO (Figure S19), the model performances of WRF-CMAQ and WRF-Chem
697 in spring and winter were slightly better than those in summer and autumn, but all
698 seasonal R values were greater than 0.89. Both WRF-CMAQ (-9.53 to -0.72 DU) and
699 WRF-Chem (-24.62 to $+10.57$ DU) had negative biases in all seasons (note: WRF-
700 Chem except for autumn). WRF-CHIMERE was better at capturing TCO in spring and
701 summer (overestimations of $+9.19$ to $+29.20$ DU) than in autumn and winter
702 (underestimations of -33.75 to -19.40 DU).

703 The R values of NO_2 columns for all three models were slightly higher in autumn
704 and winter (0.82–0.91) than in spring and summer (0.76–0.84). The simulation
705 accuracies of NO_2 columns via WRF-CHIMERE were significantly better than those
706 using WRF-CMAQ or WRF-Chem in all seasons except for winter (Figure S20). All
707 models overestimated SO_2 column concentrations in winter (by approximately 0.01–
708 0.03 DU) but underestimated them in other seasons (-0.05 to -0.001 DU) (Figure S21).

709 For NH_3 , the only primary alkaline gas in the atmosphere, better model
710 performances of WRF-CMAQ and WRF-Chem occurred in summer (R: 0.81–0.87; MB:
711 -3.42 to 2.07×10^{15} molecules cm^{-2}) (Figure S22). Ammonia emissions from fertilizer
712 and livestock have been substantially underestimated in China (Zhang et al., 2017), and
713 peak values occur in spring and summer (Huang et al., 2012). In addition, bidirectional
714 exchanges of fertilizer-induced NH_3 were not considered in our simulations.

715 WRF-CMAQ, WRF-Chem, and WRF-CHIMERE showed relatively poor
716 performances (R: 0.68–0.79) in simulating CO columns during spring, summer, and
717 autumn, respectively, compared with other seasons (Figure S23). WRF-CMAQ and
718 WRF-CHIMERE respectively underestimated and overestimated CO columns in other
719 seasons except for summer and spring, with MBs of -3.29 to 0.31×10^{17} and -0.62 to
720 2.09×10^{17} molecules cm^{-2} , respectively. WRF-Chem had positive MBs in summer and
721 autumn (4.03 – 5.12×10^{17} molecules cm^{-2}) and negative MBs in spring and winter
722 (-3.15 to -2.10×10^{17} molecules cm^{-2}).

723 Moreover, after comparing the performance results for each pollutant between
724 sections 4.1 and 4.2, the only disparity found between evaluations with ground-based
725 observations compared with those with satellite-borne observations was for CO. The
726 formation of CO via the oxidation of methane, an important source of CO emissions
727 (Stein et al., 2014), is not considered in the three coupled models, and methane
728 emissions are not included in the MEIC inventory. In addition, the contribution of CO
729 to atmospheric oxidation capacity (OH radicals) was non-negligible (e.g., values were
730 approximately 20.54%–38.97% in Beijing (Liu et al., 2021), and 26%–31% in Shanghai
731 (Zhu et al., 2020)).



732 These discrepancies in the model performances for simulating AOD and column
 733 concentrations of gases can be explained by differences in the representations of aerosol
 734 species groups, Fast-JX photolysis mechanism, and gas-phase mechanisms in the three
 735 coupled models.

736 When all three models enabled just ARI effects, improvements in annual AOD and
 737 NO₂ columns simulated by these models were relatively limited. The AOD simulations
 738 improved in spring and summer, but worsened in autumn and winter (Table 4 and Figure
 739 9). Larger variations in seasonal MBs of NO₂ columns induced by ARI effects occurred
 740 in WRF-CMAQ (−0.18 to 0.13 petamolecules cm^{−2}) compared with WRF-Chem and
 741 WRF-CHIMERE (0–0.01 petamolecules cm^{−2}). When both ARI and ACI effects were
 742 enabled in WRF-Chem, the model performance for seasonal AOD simulations
 743 worsened considerably. The annual and seasonal NO₂ simulations via WRF-Chem
 744 became slightly worse, while those using WRF-CHIMERE became slightly better. In
 745 contrast to AOD and NO₂ column concentrations, improvements in annual and seasonal
 746 column simulations of total ozone, PBL SO₂, and NH₃ via all two-way coupled models
 747 were limited when one or both of ARI and ACI were enabled.

748

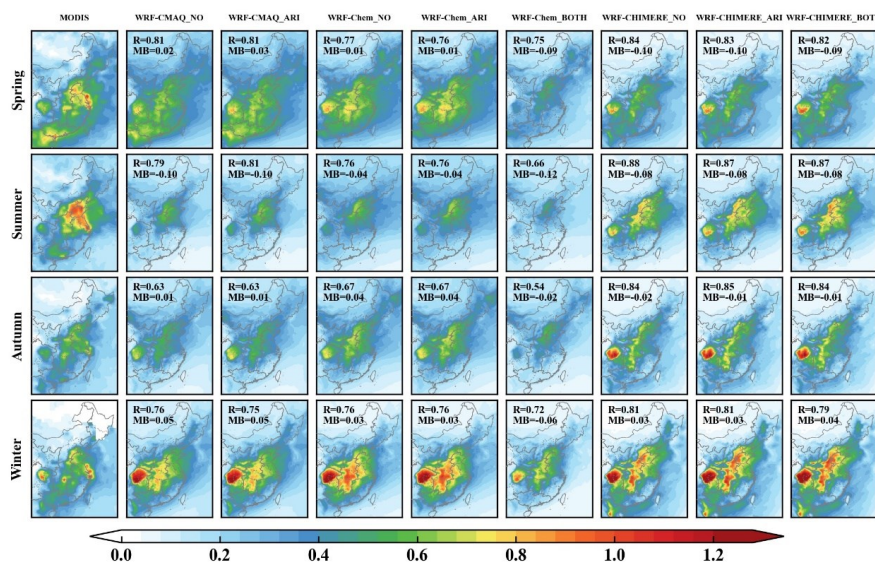
749 Table 5. Statistical metrics (R, MB, NMB, and RMSE) of simulated and satellite-
 750 retrieved AOD, total column ozone, tropospheric column NO₂, PBL column SO₂, total
 751 column CO, and total column density of NH₃ in eastern China. The best results are in
 752 bold, while annual mean simulations and observations are in italics.

Variables	Statistics	WRF-CMAQ_NO	WRF-CMAQ_ARI	WRF-Chem_NO	WRF-Chem_ARI	WRF-Chem_BOTH	WRF-CHIMERE_NO	WRF-CHIMERE_ARI	WRF-CHIMERE_BOTH
AOD (0.27)	Mean_sim	<i>0.26</i>	<i>0.27</i>	<i>0.35</i>	<i>0.36</i>	<i>0.25</i>	<i>0.21</i>	<i>0.22</i>	<i>0.22</i>
	R	0.80	0.80	0.80	0.80	0.75	0.87	0.87	0.86
	MB	-0.01	-0.01	0.09	0.09	-0.01	-0.05	-0.05	-0.04
	NMB (%)	-3.99	-2.93	34.14	35.03	-4.92	-18.72	-17.37	-16.22
	RMSE	0.09	0.09	0.15	0.15	0.10	0.09	0.09	0.10
O ₃	Mean_sim	<i>306.15</i>	<i>306.15</i>	<i>300.77</i>	<i>300.73</i>	<i>300.46</i>	<i>307.69</i>	<i>307.47</i>	<i>307.75</i>
	R	0.98	0.98	0.97	0.97	0.97	0.65	0.65	0.65
	MB	-5.92	-5.92	-10.68	-10.72	-10.99	-3.69	-3.91	-3.63
VCDs (312.07 DU)	NMB (%)	-1.90	-1.90	-3.43	-3.44	-3.53	-1.19	-1.26	-1.17
	RMSE	8.91	8.91	83.72	83.73	83.94	39.88	39.71	39.73
	Mean_sim	<i>3.80</i>	<i>3.91</i>	<i>3.07</i>	<i>3.08</i>	<i>3.06</i>	<i>2.62</i>	<i>2.63</i>	<i>2.63</i>
Tropospheric NO ₂ VCDs (2.71×10 ¹⁵ molecules cm ^{−2})	R	0.85	0.85	0.87	0.87	0.87	0.87	0.87	0.87
	MB	1.09	1.21	0.62	0.63	0.61	0.28	0.29	0.29
	NMB (%)	40.35	44.64	25.27	25.52	24.89	12.03	12.47	12.42
	RMSE	3.18	3.33	2.27	2.27	2.27	1.65	1.67	1.68
	Mean_sim	<i>0.07</i>	<i>0.07</i>	<i>0.09</i>	<i>0.09</i>	<i>0.06</i>	<i>0.06</i>	<i>0.06</i>	<i>0.06</i>
PBL SO ₂ VCDs (0.09 DU)	R	0.53	0.53	0.56	0.56	0.54	0.50	0.50	0.50
	MB	-0.03	-0.02	-0.03	-0.02	-0.03	-0.03	-0.02	-0.02
	NMB (%)	-27.32	-25.48	-32.50	-21.50	-35.08	-28.64	-27.31	-27.51
	RMSE	0.07	0.07	0.08	0.08	0.07	0.07	0.07	0.07
	Mean_sim	<i>20.34</i>	<i>20.35</i>	<i>22.20</i>	<i>22.20</i>	<i>22.21</i>	<i>22.34</i>	<i>22.36</i>	<i>22.35</i>
Total CO VCDs	R	0.83	0.83	0.87	0.87	0.87	0.86	0.86	0.86



$(21.60 \times 10^{17}$ molecules cm ⁻²)	MB	-1.26	-1.24	0.93	0.93	0.94	1.19	1.21	1.19
	NMB (%)	-5.83	-5.75	4.35	4.37	4.44	5.64	5.70	5.65
	RMSE	2.54	2.54	2.69	2.68	2.69	2.57	2.58	2.58
Total NH ₃ VCDs $(16.05 \times 10^{15}$ molecules cm ⁻²)	Mean_sim	<i>13.06</i>	<i>13.15</i>	<i>12.31</i>	<i>12.27</i>	<i>8.63</i>	NA	NA	NA
	R	0.76	0.76	0.73	0.73	0.76	NA	NA	NA
	MB	-3.00	-2.90	-3.27	-3.32	-3.34	NA	NA	NA
	NMB (%)	-18.66	-18.08	-21.01	-21.28	-21.41	NA	NA	NA
	RMSE	9.26	9.47	9.48	9.46	9.61	NA	NA	NA

753 NA indicates that outputs of NH₃ column concentrations were not extracted from WRF-CHIMERE
 754 with/without aerosol feedback simulations.



755
 756 Figure 8. Spatial distributions of seasonal AOD between MODIS observations and
 757 simulations from WRF-CMAQ, WRF-Chem, and WRF-CHIMERE with and without
 758 aerosol feedbacks in eastern China.

759
 760 4.3 Computational performance

761 Table 5 summarizes the comparative results of central processing unit (CPU) time
 762 consumption for one day simulations via WRF-CMAQ, WRF-Chem, and WRF-
 763 CHIMERE with and without aerosol feedbacks in 2017. The results show that
 764 regardless of whether aerosol feedbacks were enabled, the CPU time consumed by
 765 WRF-CMAQ simulating one-day meteorology and air quality was shortest, followed
 766 by WRF-CHIMERE, and WRF-Chem. Compared with simulations without aerosol
 767 feedbacks, the processing time of WRF-CMAQ with ARI enabled increased by 0.22–
 768 0.34 hours per day, while increases in the running time of WRF-Chem and WRF-
 769 CHIMERE were not significant (0.02–0.03 hours per day). The CPU time for both
 770 WRF-Chem and WRF-CHIMERE with both ARI and ACI effects enabled was slightly



771 increased, and the increase in CPU time for the former (0.25 hours per day) was larger
772 than that for the latter (0.11 hours per day). Compared with WRF-CMAQ and WRF-
773 Chem, the CPU time of WRF-CHIMERE showed obvious seasonal differences, with
774 the time in winter and spring being significantly longer than that in summer and autumn.
775 These differences can be partially explained by the choice of main configurations,
776 including model resolution, model version, and parametrization schemes (cloud
777 microphysics, PBL, cumulus, surface layer, land surface, gas-phase chemistry, and
778 aerosol mechanisms).

779 Table 5. Summary of running time for different coupled models.

Month	WRF-CMAQ (hour)		WRF-Chem (hour)			WRF-CHIMERE (hour)		
	NO	ARI	NO	ARI	BOTH	NO	ARI	BOTH
Jan.	0.37	0.59	0.69	0.71	0.96	0.67	0.70	0.77
Feb.	0.35	0.60	0.68	0.70	0.93	0.64	0.67	0.73
Mar.	0.39	0.65	0.70	0.72	1.00	0.59	0.62	0.72
Apr.	0.37	0.67	0.67	0.69	0.92	0.54	0.57	0.65
May	0.39	0.71	0.61	0.66	0.86	0.52	0.55	0.62
June	0.40	0.74	0.66	0.67	0.95	0.48	0.51	0.63
July	0.36	0.69	0.65	0.67	0.86	0.49	0.50	0.58
Aug.	0.38	0.68	0.66	0.68	0.90	0.49	0.52	0.61
Sept.	0.37	0.63	0.64	0.65	0.89	0.48	0.52	0.63
Oct.	0.38	0.62	0.66	0.68	0.94	0.53	0.56	0.69
Nov.	0.36	0.58	0.68	0.70	0.91	0.64	0.67	0.72
Dec.	0.35	0.57	0.63	0.66	0.87	0.67	0.70	0.74

780

781 5 Conclusions

782 In this study, we comprehensively evaluated the annual hindcast simulations for
783 2017 by the two-way coupled WRF-CMAQ, WRF-Chem, and WRF-CHIMERE
784 models with/without aerosol feedbacks and explored the impacts of ARI and/or ACI on
785 model and computational performances in eastern China. All three two-way coupled
786 models effectively reproduced the spatiotemporal distributions of meteorology and air
787 quality, but some variables (SSR and $PM_{2.5}$) in specific regions showed significant
788 discrepancies. Among meteorological variables at the annual scale, T2 and Q2 were
789 better simulated by the three models than SSR, RH2, WS10, PBLH, and PREP. The
790 SSR, RH2, and WS10 were overestimated with MBs around $15.91\text{--}42.65\text{ W m}^{-2}$, 2.53--
791 3.55% and $0.42\text{--}1.04\text{ m s}^{-1}$, respectively, while T2 and Q2 were underestimated with
792 MBs ranged from -0.57 to -0.18 g kg^{-1} and -2.00 to $0.68\text{ }^{\circ}\text{C}$, respectively. For PREP, the
793 WRF-CMAQ's underestimation was 0.5 mm day^{-1} , but WRF-Chem and WRF-
794 CHIMERE overestimated PREP about 1 mm day^{-1} . The seasonal variations of
795 simulated meteorological variables in eastern China were also well matched with
796 observations. Overall, the MBs of every meteorological variable simulated by the three
797 models in spring and winter were significantly smaller than those in summer and
798 autumn. In terms of air quality, all three models presented generally acceptable



799 performance for annual surface PM_{2.5}, O₃, and NO₂ concentrations, but not for SO₂ and
800 CO. The overall performances of WRF-CMAQ were best, followed by WRF-Chem,
801 and WRF-CHIMERE. The WRF-CMAQ and WRF-Chem simulations had positive
802 biases for NO₂ (2.74–3.26 μg m⁻³) and O₃ (25.58–26.30 μg m⁻³), but negative biases for
803 other pollutants, while WRF-CHIMERE simulations had positive biases for PM_{2.5}
804 (17.18–20.37 μg m⁻³) and O₃ (14.25–14.69 μg m⁻³). The seasonal simulations of surface
805 air quality variables showed better correlations of PM_{2.5}, NO₂, SO₂, and CO in winter,
806 and O₃ in summer than those in other seasons. Further compared with satellite
807 observations, all coupled models well captured radiation, precipitation, cloud fraction,
808 AOD, and column concentrations of O₃, NO₂, CO, and NH₃ both at annual and seasonal
809 scales, but not for LWP and SO₂ concentrations.

810 Our evaluations showed that the effects of aerosol feedbacks on model
811 performances varied depending on the two-way coupled models, variables, and time
812 scales. In general, all three two-way coupled models enabling ARI improved the
813 simulation accuracy of annual and seasonal SSR. However, simulation accuracy of SSR
814 was reduced in WRF-Chem and WRF-CHIMERE with only considering ACI, with
815 slightly improved results after enabling both ARI and ACI. Aerosol feedbacks induced
816 various changes of MB for different variables. For example, MBs decreased for SSR
817 from -19.98 W m⁻² to -9.24 W m⁻², T2 from -0.20 °C to -0.15 °C, Q2 from -0.17 g kg⁻¹
818 to -0.02 g kg⁻¹, WS10 from -0.03 m s⁻¹ to -0.01 m s⁻¹ and PBLH from -25.25 m to -1.93
819 m. MBs increased for PM_{2.5} from 1.53 to 3.19 μg m⁻³ and other gaseous pollutants (NO₂,
820 SO₂ and CO) as well. In addition, there were computational costs (around 20%–70%
821 increase) involved with turning on aerosol-radiation-cloud effects in two-way coupled
822 models.

823 Although many progresses in the developments and enhancements of two-way
824 coupled models have been made and these models are widely applied worldwide,
825 several limitations still exist. As comparison studies of offline models' performances
826 affected by various chemical mechanisms were conducted (Kim et al., 2011; Balzarini
827 et al., 2015; Zheng et al., 2015), relevant assessments targeting two-way coupled
828 models are still lacking. Recently, Wu et al. (2018) and Womack et al. (2021)
829 demonstrated that the non-spherical morphology of BC particles could significantly
830 enhance light absorption and the spherical core-shell mixing assumptions used in the
831 most applied coupled models (WRF-CMAQ, WRF-Chem, and WRF-CHIMERE) may
832 overestimate the ARI effects of BC aerosols. Therefore, numerical representations of
833 non-spherical aerosol optical properties need to be implemented in two-way coupled
834 models to reduce uncertainties in the ARI calculations. Previous observational and
835 modeling studies revealed that there are still large uncertainties in the impacts of ACI
836 on cloud and precipitation (Seinfeld et al., 2016; IPCC, 2021; Gao et al., 2022), and
837 more researchers have focused on these gaps and gained some remarkable
838 developments on aerosol water uptake and in-/below-cloud scavenging in recent years
839 (Xu et al., 2019; Brüggemann et al., 2020; Kärcher and Marcolli, 2021; Cantrell et al.,
840 2022; Ryu and Min, 2022; Hogrefe et al., 2023). The latest observational investigations
841 for coefficient modifications and newly developed parameterizations/schemes need to
842 be incorporated into the two-way coupled models, such as WRF-CMAQ, WRF-Chem



843 and WRF-CHIMERE, and further reassessments of uncertainties of the ACI effects in
844 these models should be carried out in the future.

845

846 Code availability

847 The source codes of the two-way coupled WRF v4.1.1-CMAQ v5.3.1, WRF-
848 Chem v4.1.1, and WRF v3.7.1-CHIMERE v2020r1 models are obtained from
849 <https://github.com/USEPA/CMAQ>, <https://github.com/wrf-model/WRF>, and
850 <https://www.lmd.polytechnique.fr/chimere>, respectively (last access: November 2020).
851

852 Data availability

853 The model inputs and outputs in this study for WRF-CMAQ, WRF-Chem and
854 WRF-CHIMERE with/without enabling ARI or/and ACI effects are available upon
855 request. All simulation and observational data of ground-based/satellite-retrieved
856 meteorological and air quality for computing statistical metrics are available from
857 <https://zenodo.org/record/7750907> (last access: 20 March, 2023).
858

859 Author contributions

860 CG, ZX, AX performed the majority of the source code configuration of WRF-
861 CMAQ, WRF-Chem and WRF-CHIMERE, designed the numerical simulations to
862 carry them out, related analysis, figure plotting, and paper writing. QT, HZ, SZ, GY,
863 MZ and XS were involved with the original research plan and made suggestions for the
864 paper writing.
865

866 Competing interests

867 The contact author has declared that neither they nor their co-authors have any
868 competing interests.
869

870 Acknowledgements

871 The authors are very grateful to David Wong, Chun Zhao and Laurent Menut who
872 provided detailed information on the two-way coupled WRF-CMAQ, WRF-Chem and
873 WRF-CHIMERE models, respectively.
874

875 Financial support

876 This study was financially sponsored by the Youth Innovation Promotion
877 Association of Chinese Academy of Sciences, China (grant nos. 2022230), the National
878 Key Research and Development Program of China (grant nos. 2017YFC0212304 &
879 2019YFE0194500), the Talent Program of Chinese Academy of Sciences
880 (Y8H1021001), and the National Natural Science Foundation of China (grant nos.
881 42171142 & 41771071).
882

883



884 References

- 885 Alapaty, K., Herwehe, J. A., Otte, T. L., Nolte, C. G., Bullock, O. R., Mallard, M. S., Kain, J. S.,
886 and Dudhia, J.: Introducing subgrid-scale cloud feedbacks to radiation for regional
887 meteorological and climate modeling, *Geophys. Res. Lett.*, 39, 1–5,
888 <https://doi.org/10.1029/2012GL054031>, 2012.
- 889 Baklanov, A., Schlünzen, K., Suppan, P., Baldasano, J., Brunner, D., Aksoyoglu, S., Carmichael,
890 G., Douros, J., Flemming, J., and Forkel, R.: Online coupled regional meteorology chemistry
891 models in Europe: current status and prospects, *Atmos. Chem. Phys.*, 14, 317–398,
892 <https://doi.org/10.5194/acp-14-317-2014>, 2014.
- 893 Balzarini, A., Pirovano, G., Honzak, L., Žabkar, R., Curci, G., Forkel, R., Hirtl, M., San José, R.,
894 Tuccella, P., and Grell, G. A.: WRF-Chem model sensitivity to chemical mechanisms choice
895 in reconstructing aerosol optical properties, *Atmos. Environ.*, 115, 604–619,
896 <https://doi.org/10.1016/j.atmosenv.2014.12.033>, 2015.
- 897 Briant, R., Tuccella, P., Deroubaix, A., Khvorostyanov, D., Menut, L., Mailler, S., and Turquety,
898 S.: Aerosol-radiation interaction modelling using online coupling between the WRF 3.7.1
899 meteorological model and the CHIMERE 2016 chemistry-transport model, through the
900 OASIS3-MCT coupler, *Geosci. Model Dev.*, 10, 927–944, <https://doi.org/10.5194/gmd-10-927-2017>, 2017.
- 902 Brüggemann, M., Xu, R., Tilgner, A., Kwong, K. C., Mutzel, A., Poon, H. Y., Otto, T., Schaefer,
903 T., Poulain, L., and Chan, M. N.: Organosulfates in ambient aerosol: state of knowledge and
904 future research directions on formation, abundance, fate, and importance, *Environ. Sci.
905 Technol.*, 54, 3767–3782, <https://doi.org/10.1021/acs.est.9b06751>, 2020.
- 906 Brunner, D., Savage, N., Jorba, O., Eder, B., Giordano, L., Badia, A., Balzarini, A., Baro, R.,
907 Bianconi, R., and Chemel, C.: Comparative analysis of meteorological performance of coupled
908 chemistry-meteorology models in the context of AQMEII phase 2, *Atmos. Environ.*, 115, 470–
909 498, <https://doi.org/10.1016/j.atmosenv.2014.12.032>, 2015.
- 910 Campbell, P., Zhang, Y., Wang, K., Leung, R., Fan, J., Zheng, B., Zhang, Q., and He, K.: Evaluation
911 of a multi-scale WRF-CAM5 simulation during the 2010 East Asian Summer Monsoon, *Atmos.
912 Environ.*, 169, 204–217, <https://doi.org/10.1016/j.atmosenv.2017.09.008>, 2017.
- 913 Cantrell, W., Shaw, R., and Mazzoleni, C.: Final Technical Report for “Laboratory Measurements
914 of Cloud Scavenging of Interstitial Aerosol in a Turbulent Environment”, DE-SC0018931,
915 Michigan Technological Univ., Houghton, MI (United States), 2022.
- 916 Carslaw, K. S., Boucher, O., Spracklen, D. V., Mann, G. W., Rae, J. G. L., Woodward, S., and
917 Kulmala, M.: A review of natural aerosol interactions and feedbacks within the Earth system,
918 *Atmos. Chem. Phys.*, 10, 1701–1737, <https://doi.org/10.5194/acp-10-1701-2010>, 2010.
- 919 Chen, L., Gao, Y., Zhang, M., Fu, J. S., Zhu, J., Liao, H., Li, J., Huang, K., Ge, B., and Wang, X.:
920 MICS-Asia III: Multi-model comparison and evaluation of aerosol over East Asia, *Atmos.
921 Chem. Phys.*, 19, 11911–11937, <https://doi.org/10.5194/acp-19-11911-2019>, 2019.
- 922 Ding, Q. J., Sun, J., Huang, X., Ding, A., Zou, J., Yang, X., and Fu, C.: Impacts of black carbon on
923 the formation of advection–radiation fog during a haze pollution episode in eastern China,
924 *Atmos. Chem. Phys.*, 19, 7759–7774, <https://doi.org/10.5194/acp-19-7759-2019>, 2019.
- 925 Dionne, J., von Salzen, K., Cole, J., Mahmood, R., Leaitch, W. R., Lesins, G., Folkens, I., and Chang,
926 R. Y.-W.: Modelling the relationship between liquid water content and cloud droplet number
927 concentration observed in low clouds in the summer Arctic and its radiative effects, *Atmos.*



- 928 Chem. Phys., 20, 29–43, <https://doi.org/10.5194/acp-20-29-2020>, 2020.
- 929 Fan, J., Wang, Y., Rosenfeld, D., and Liu, X.: Review of aerosol-cloud interactions: Mechanisms,
930 significance, and challenges, *J. Atmos. Sci.*, 73, 4221–4252, [https://doi.org/10.1175/JAS-D-](https://doi.org/10.1175/JAS-D-16-0037.1)
931 16-0037.1, 2016.
- 932 Feng, X., Lin, H., Fu, T.-M., Sulprizio, M. P., Zhuang, J., Jacob, D. J., Tian, H., Ma, Y., Zhang, L.,
933 and Wang, X.: WRF-GC (v2.0): online two-way coupling of WRF (v3.9.1.1) and GEOS-Chem
934 (v12.7.2) for modeling regional atmospheric chemistry–meteorology interactions, *Geosci.*
935 *Model Dev.*, 14, 3741–3768, <https://doi.org/10.5194/gmd-14-3741-2021>, 2021.
- 936 Gao, C., Zhang, X., Xiu, A., Huang, L., Zhao, H., Wang, K., and Tong, Q.: Spatiotemporal
937 distribution of biogenic volatile organic compounds emissions in China, *Acta Sci.*
938 *Circumstantiae*, 39, 4140–4151, <https://doi.org/10.13671/j.hjkxxb.2019.0243>, 2019.
- 939 Gao, C., Xiu, A., Zhang, X., Tong, Q., Zhao, H., Zhang, S., Yang, G., and Zhang, M.: Two-way
940 coupled meteorology and air quality models in Asia: a systematic review and meta-analysis of
941 impacts of aerosol feedbacks on meteorology and air quality, *Atmos. Chem. Phys.*, 22, 5265–
942 5329, <https://doi.org/10.5194/acp-22-5265-2022>, 2022.
- 943 Gao, J., Woodward, A., Vardoulakis, S., Kovats, S., Wilkinson, P., Li, L., Xu, L., Li, J., Yang, J.,
944 and Cao, L.: Haze, public health and mitigation measures in China: A review of the current
945 evidence for further policy response, *Sci. Total Environ.*, 578, 148–157,
946 <https://doi.org/10.1016/j.scitotenv.2016.10.231>, 2017.
- 947 Gao, M., Han, Z., Liu, Z., Li, M., Xin, J., Tao, Z., Li, J., Kang, J. E., Huang, K., Dong, X., Zhuang,
948 B., Li, S., Ge, B., Wu, Q., Cheng, Y., Wang, Y., Lee, H. J., Kim, C. H., Fu, J. S., Wang, T.,
949 Chin, M., Woo, J. H., Zhang, Q., Wang, Z., and Carmichael, G. R.: Air quality and climate
950 change, Topic 3 of the Model Inter-Comparison Study for Asia Phase III (MICS-Asia III)- Part
951 1: Overview and model evaluation, *Atmos. Chem. Phys.*, 18, 4859–4884,
952 <https://doi.org/10.5194/acp-18-4859-2018>, 2018.
- 953 Gao, M., Han, Z., Tao, Z., Li, J., Kang, J.-E., Huang, K., Dong, X., Zhuang, B., Li, S., and Ge, B.:
954 Air quality and climate change, Topic 3 of the Model Inter-Comparison Study for Asia Phase
955 III (MICS-Asia III)–Part 2: aerosol radiative effects and aerosol feedbacks, *Atmos. Chem.*
956 *Phys.*, 20, 1147–1161, <https://doi.org/10.5194/acp-20-1147-2020>, 2020.
- 957 Gao, Y., Zhang, M., Liu, Z., Wang, L., Wang, P., Xia, X., Tao, M., and Zhu, L.: Modeling the
958 feedback between aerosol and meteorological variables in the atmospheric boundary layer
959 during a severe fog-haze event over the North China Plain., *Atmos. Chem. Phys.*, 15, 4279–
960 4295, <https://doi.org/10.5194/acp-15-4279-2015>, 2015.
- 961 Ge, B., Itahashi, S., Sato, K., Xu, D., Wang, J., Fan, F., Tan, Q., Fu, J. S., Wang, X., and Yamaji,
962 K.: Model Inter-Comparison Study for Asia (MICS-Asia) phase III: multimodel comparison
963 of reactive nitrogen deposition over China, *Atmos. Chem. Phys.*, 20, 10587–10610,
964 <https://doi.org/10.5194/acp-20-10587-2020>, 2020.
- 965 Geng, G., Zheng, Y., Zhang, Q., Xue, T., Zhao, H., Tong, D., Zheng, B., Li, M., Liu, F., and Hong,
966 C.: Drivers of PM_{2.5} air pollution deaths in China 2002–2017, *Nat. Geosci.*, 14, 645–650,
967 <https://doi.org/10.1038/s41561-021-00792-3>, 2021.
- 968 Gillies, S., Ward, B., and Petersen, A. S.: Rasterio: Geospatial raster I/O for Python programmers,
969 URL <https://github.com/mapbox/rasterio>, 2013.
- 970 Govardhan, G. R., Nanjundiah, R. S., Satheesh, S. K., Moorthy, K. K., and Takemura, T.: Inter-
971 comparison and performance evaluation of chemistry transport models over Indian region,



- 972 Atmos. Environ., 125, 486–504, <https://doi.org/10.1016/j.atmosenv.2015.10.065>, 2016.
- 973 Grell, G. and Baklanov, A.: Integrated modeling for forecasting weather and air quality: A call for
974 fully coupled approaches, Atmos. Environ., 45, 6845–6851,
975 <https://doi.org/10.1016/j.atmosenv.2011.01.017>, 2011.
- 976 Grell, G. A., Peckham, S. E., Schmitz, R., McKeen, S. A., Frost, G., Skamarock, W. C., and Eder,
977 B.: Fully coupled “online” chemistry within the WRF model, Atmos. Environ., 39, 6957–6975,
978 <https://doi.org/10.1016/j.atmosenv.2005.04.027>, 2005.
- 979 Guo, J., Miao, Y., Zhang, Y., Liu, H., Li, Z., Zhang, W., He, J., Lou, M., Yan, Y., and Bian, L.: The
980 climatology of planetary boundary layer height in China derived from radiosonde and
981 reanalysis data, Atmos. Chem. Phys., 16, 13309–13319, [https://doi.org/10.5194/acp-16-13309-](https://doi.org/10.5194/acp-16-13309-2016)
982 2016, 2016.
- 983 Guo, J., Li, Y., Cohen, J. B., Li, J., Chen, D., Xu, H., Liu, L., Yin, J., Hu, K., and Zhai, P.: Shift in
984 the temporal trend of boundary layer height in China using long-term (1979–2016) radiosonde
985 data, Geophys. Res. Lett., 46, 6080–6089, <https://doi.org/10.1029/2019GL082666>, 2019.
- 986 He, J., Zhang, Y., Wang, K., Chen, Y., Leung, L. R., Fan, J., Li, M., Zheng, B., Zhang, Q., and
987 Duan, F.: Multi-year application of WRF-CAM5 over East Asia-Part I: Comprehensive
988 evaluation and formation regimes of O₃ and PM_{2.5}, Atmos. Environ., 165, 122–142,
989 <https://doi.org/10.1016/j.atmosenv.2017.06.015>, 2017.
- 990 He, K., Huo, H., and Zhang, Q.: Urban air pollution in China: current status, characteristics, and
991 progress, Annu. Rev. Environ. Resour., 27, 397,
992 <https://doi.org/10.1146/annurev.energy.27.122001.083421>, 2002.
- 993 Hogrefe, C., Bash, J. O., Pleim, J. E., Schwede, D. B., Gilliam, R. C., Foley, K. M., Appel, K. W.,
994 and Mathur, R.: An Analysis of CMAQ Gas Phase Dry Deposition over North America
995 Through Grid-Scale and Land-Use Specific Diagnostics in the Context of AQMEII4, Atmos.
996 Chem. Phys. Discuss., 1–52, <https://doi.org/10.5194/acp-2023-10>, 2023.
- 997 Hong, C., Zhang, Q., Zhang, Y., Tang, Y., Tong, D., and He, K.: Multi-year downscaling application
998 of two-way coupled WRF v3.4 and CMAQ v5.0.2 over east Asia for regional climate and air
999 quality modeling: model evaluation and aerosol direct effects., Geosci. Model Dev., 10, 2447–
1000 2470, <https://doi.org/10.5194/gmd-10-2447-2017>, 2017.
- 1001 Huang, D. and Gao, S.: Impact of different reanalysis data on WRF dynamical downscaling over
1002 China, Atmos. Res., 200, 25–35, <https://doi.org/10.1016/j.atmosres.2017.09.017>, 2018.
- 1003 Im, U., Bianconi, R., Solazzo, E., Kioutsioukis, I., Badia, A., Balzarini, A., Baró, R., Bellasio, R.,
1004 Brunner, D., and Chemel, C.: Evaluation of operational on-line-coupled regional air quality
1005 models over Europe and North America in the context of AQMEII phase 2. Part I: Ozone,
1006 Atmos. Environ., 115, 404–420, <https://doi.org/10.1016/j.atmosenv.2014.09.042>, 2015a.
- 1007 Im, U., Bianconi, R., Solazzo, E., Kioutsioukis, I., Badia, A., Balzarini, A., Baró, R., Bellasio, R.,
1008 Brunner, D., and Chemel, C.: Evaluation of operational online-coupled regional air quality
1009 models over Europe and North America in the context of AQMEII phase 2. Part II: Particulate
1010 matter, Atmos. Environ., 115, 421–441, <https://doi.org/10.1016/j.atmosenv.2014.08.072>,
1011 2015b.
- 1012 IPCC: Climate change 2007: Synthesis Report. Contribution of Working Groups I, II and III to the
1013 Fourth Assessment Report of the Intergovernmental Panel on Climate Change, 2007.
- 1014 IPCC: Climate change 2021: Synthesis Report. Contribution of Working Groups I, II and III to the
1015 Sixth Assessment Report of the Intergovernmental Panel on Climate Change., 2021.



- 1016 Itahashi, S., Ge, B., Sato, K., Fu, J. S., Wang, X., Yamaji, K., Nagashima, T., Li, J., Kajino, M., and
1017 Liao, H.: MICS-Asia III: overview of model intercomparison and evaluation of acid deposition
1018 over Asia, *Atmos. Chem. Phys.*, 20, 2667–2693, <https://doi.org/10.5194/acp-20-2667-2020>,
1019 2020.
- 1020 Jacobson, M. Z.: Analysis of aerosol interactions with numerical techniques for solving coagulation,
1021 nucleation, condensation, dissolution, and reversible chemistry among multiple size
1022 distributions, *J. Geophys. Res. Atmos.*, 107, AAC-2, <https://doi.org/10.1029/2001JD002044>,
1023 2002.
- 1024 Kärcher, B. and Marcolli, C.: Aerosol–cloud interactions: the representation of heterogeneous ice
1025 activation in cloud models, *Atmos. Chem. Phys.*, 21, 15213–15220,
1026 <https://doi.org/10.5194/acp-21-15213-2021>, 2021.
- 1027 Keita, S. A., Girard, E., Raut, J.-C., Leriche, M., Blanchet, J.-P., Pelon, J., Onishi, T., and Cirisan,
1028 A.: A new parameterization of ice heterogeneous nucleation coupled to aerosol chemistry in
1029 WRF-Chem model version 3.5.1: evaluation through ISDAC measurements, *Geosci. Model*
1030 *Dev.*, 13, 5737–5755, <https://doi.org/10.5194/gmd-13-5737-2020>, 2020.
- 1031 Kim, Y., Sartelet, K., and Seigneur, C.: Formation of secondary aerosols over Europe: comparison
1032 of two gas-phase chemical mechanisms, *Atmos. Chem. Phys.*, 11, 583–598,
1033 <https://doi.org/10.5194/acp-11-583-2011>, 2011.
- 1034 Klein, S. A., McCoy, R. B., Morrison, H., Ackerman, A. S., Avramov, A., Boer, G. de, Chen, M.,
1035 Cole, J. N. S., Del Genio, A. D., and Falk, M.: Intercomparison of model simulations of mixed-
1036 phase clouds observed during the ARM Mixed-Phase Arctic Cloud Experiment. I: Single-layer
1037 cloud, *Q. J. R. Meteorol. Soc. A J. Atmos. Sci. Appl. Meteorol. Phys. Oceanogr.*, 135, 979–
1038 1002, <https://doi.org/10.1002/qj.416>, 2009.
- 1039 Knote, C., Tuccella, P., Curci, G., Emmons, L., Orlando, J. J., Madronich, S., Baró, R., Jiménez-
1040 Guerrero, P., Luecken, D., and Hogrefe, C.: Influence of the choice of gas-phase mechanism
1041 on predictions of key gaseous pollutants during the AQMEII phase-2 intercomparison, *Atmos.*
1042 *Environ.*, 115, 553–568, <https://doi.org/10.1016/j.atmosenv.2014.11.066>, 2015.
- 1043 Kong, L., Tang, X., Zhu, J., Wang, Z., Fu, J. S., Wang, X., Itahashi, S., Yamaji, K., Nagashima, T.,
1044 and Lee, H.-J.: Evaluation and uncertainty investigation of the NO₂, CO and NH₃ modeling
1045 over China under the framework of MICS-Asia III, *Atmos. Chem. Phys.*, 20, 181–202,
1046 <https://doi.org/10.5194/acp-20-181-2020>, 2020.
- 1047 Li, D., Xue, L., Wen, L., Wang, X., Chen, T., Mellouki, A., Chen, J., and Wang, W.: Characteristics
1048 and sources of nitrous acid in an urban atmosphere of northern China: Results from 1-yr
1049 continuous observations, *Atmos. Environ.*, 182, 296–306,
1050 <https://doi.org/10.1016/j.atmosenv.2018.03.033>, 2018.
- 1051 Li, J., Nagashima, T., Kong, L., Ge, B., Yamaji, K., Fu, J. S., Wang, X., Fan, Q., Itahashi, S., and
1052 Hyo-Jung, L.: Model evaluation and intercomparison of surface-level ozone and relevant
1053 species in East Asia in the context of MICS-Asia Phase III–Part 1: Overview, *Atmos. Chem.*
1054 *Phys.*, 19, 12993–13015, <https://doi.org/10.5194/acp-19-12993-2019>, 2019.
- 1055 Li, M., Liu, H., Geng, G., Hong, C., Liu, F., Song, Y., Tong, D., Zheng, B., Cui, H., and Man, H.:
1056 Anthropogenic emission inventories in China: a review, *Natl. Sci. Rev.*, 4, 834–866,
1057 <https://doi.org/10.1093/nsr/nwx150>, 2017.
- 1058 Liu, X.-H., Zhang, Y., Cheng, S.-H., Xing, J., Zhang, Q., Streets, D. G., Jang, C., Wang, W.-X., and
1059 Hao, J.-M.: Understanding of regional air pollution over China using CMAQ, part I



- 1060 performance evaluation and seasonal variation, *Atmos. Environ.*, 44, 2415–2426,
1061 <https://doi.org/10.1016/j.atmosenv.2010.03.035>, 2010.
- 1062 Liu, Y., Lu, K., Li, X., Dong, H., Tan, Z., Wang, H., Zou, Q., Wu, Y., Zeng, L., and Hu, M.: A
1063 comprehensive model test of the HONO sources constrained to field measurements at rural
1064 North China Plain, *Environ. Sci. Technol.*, 53, 3517–3525,
1065 <https://doi.org/10.1021/acs.est.8b06367>, 2019.
- 1066 Liu, Z., Wang, Y., Hu, B., Lu, K., Tang, G., Ji, D., Yang, X., Gao, W., Xie, Y., and Liu, J.:
1067 Elucidating the quantitative characterization of atmospheric oxidation capacity in Beijing,
1068 China, *Sci. Total Environ.*, 771, 145306, <https://doi.org/10.1016/j.scitotenv.2021.145306>,
1069 2021.
- 1070 López-Romero, J. M., Montávez, J. P., Jerez, S., Lorente-Plazas, R., Palacios-Peña, L., and Jiménez-
1071 Guerrero, P.: Precipitation response to aerosol–radiation and aerosol–cloud interactions in
1072 regional climate simulations over Europe, *Atmos. Chem. Phys.*, 21, 415–430,
1073 <https://doi.org/10.5194/acp-21-415-2021>, 2021.
- 1074 Ma, Y., Jin, Y., Zhang, M., Gong, W., Hong, J., Jin, S., Shi, Y., Zhang, Y., and Liu, B.: Aerosol
1075 optical properties of haze episodes in eastern China based on remote-sensing observations and
1076 WRF-Chem simulations, *Sci. Total Environ.*, 757, 143784,
1077 <https://doi.org/10.1016/j.scitotenv.2020.143784>, 2021.
- 1078 Makar, P. A., Gong, W., Milbrandt, J., Hogrefe, C., Zhang, Y., Curci, G., Žabkar, R., Im, U.,
1079 Balzarini, A., Baró, R., Bianconi, R., Cheung, P., Forkel, R., Gravel, S., Hirtl, M., Honzak, L.,
1080 Hou, A., Jiménez-Guerrero, P., Langer, M., Moran, M. D., Pabla, B., Pérez, J. L., Pirovano, G.,
1081 San José, R., Tuccella, P., Werhahn, J., Zhang, J., and Galmarini, S.: Feedbacks between air
1082 pollution and weather, Part 1: Effects on weather, *Atmos. Environ.*, 115, 442–469,
1083 <https://doi.org/10.1016/j.atmosenv.2014.12.003>, 2015a.
- 1084 Makar, P. A., Gong, W., Hogrefe, C., Zhang, Y., Curci, G., Žabkar, R., Milbrandt, J., Im, U.,
1085 Balzarini, A., Baró, R., Bianconi, R., Cheung, P., Forkel, R., Gravel, S., Hirtl, M., Honzak, L.,
1086 Hou, A., Jiménez-Guerrero, P., Langer, M., Moran, M. D., Pabla, B., Pérez, J. L., Pirovano, G.,
1087 San José, R., Tuccella, P., Werhahn, J., Zhang, J., and Galmarini, S.: Feedbacks between air
1088 pollution and weather, part 2: Effects on chemistry, *Atmos. Environ.*, 115, 499–526,
1089 <https://doi.org/10.1016/j.atmosenv.2014.10.021>, 2015b.
- 1090 Qu, Y., Voulgarakis, A., Wang, T., Kasoar, M., Wells, C., Yuan, C., Varma, S., and Mansfield, L.:
1091 A study of the effect of aerosols on surface ozone through meteorology feedbacks over China,
1092 *Atmos. Chem. Phys.*, 21, 5705–5718, <https://doi.org/10.5194/acp-21-5705-2021>, 2021.
- 1093 Rosenfeld, D., Andreae, M. O., Asmi, A., Chin, M., de Leeuw, G., Donovan, D. P., Kahn, R., Kinne,
1094 S., Kivekäs, N., and Kulmala, M.: Global observations of aerosol–cloud–precipitation–climate
1095 interactions, *Rev. Geophys.*, 52, 750–808, <https://doi.org/10.1002/2013RG000441>, 2014.
- 1096 Ryu, Y. and Min, S.: Improving Wet and Dry Deposition of Aerosols in WRF-Chem: Updates to
1097 Below-Cloud Scavenging and Coarse-Particle Dry Deposition, *J. Adv. Model. Earth Syst.*, 14,
1098 e2021MS002792, <https://doi.org/10.1029/2021MS002792>, 2022.
- 1099 Seinfeld, J. H., Bretherton, C., Carslaw, K. S., Coe, H., DeMott, P. J., Dunlea, E. J., Feingold, G.,
1100 Ghan, S., Guenther, A. B., and Kahn, R.: Improving our fundamental understanding of the role
1101 of aerosol–cloud interactions in the climate system, *Proc. Natl. Acad. Sci.*, 113, 5781–5790,
1102 <https://doi.org/10.1073/pnas.1514043113>, 2016.
- 1103 Spataro, F., Ianniello, A., Esposito, G., Allegrini, I., Zhu, T., and Hu, M.: Occurrence of atmospheric



- 1104 nitrous acid in the urban area of Beijing (China), *Sci. Total Environ.*, 447, 210–224,
1105 <https://doi.org/10.1016/j.scitotenv.2012.12.065>, 2013.
- 1106 Stein, O., Schultz, M. G., Bouarar, I., Clark, H., Huijnen, V., Gaudel, A., George, M., and Clerbaux,
1107 C.: On the wintertime low bias of Northern Hemisphere carbon monoxide found in global
1108 model simulations, *Atmos. Chem. Phys.*, 14, 9295–9316, [https://doi.org/10.5194/acp-14-9295-](https://doi.org/10.5194/acp-14-9295-2014)
1109 2014, 2014.
- 1110 Tang, W., Yang, K., Qin, J., Li, X., and Niu, X.: A 16-year dataset (2000–2015) of high-resolution
1111 (3 h, 10 km) global surface solar radiation, *Earth Syst. Sci. Data*, 11, 1905–1915,
1112 <https://doi.org/10.5194/essd-11-1905-2019>, 2019.
- 1113 Tuccella, P., Menut, L., Briant, R., Deroubaix, A., Khvorostyanov, D., Mailler, S., Siour, G., and
1114 Turquety, S.: Implementation of aerosol-cloud interaction within WRF-CHIMERE online
1115 coupled model: Evaluation and investigation of the indirect radiative effect from anthropogenic
1116 emission reduction on the Benelux Union, *Atmosphere (Basel)*, 10,
1117 <https://doi.org/10.3390/atmos10010020>, 2019.
- 1118 Wallace, J. M. and Hobbs, P. V.: *Atmospheric science: an introductory survey*, Elsevier, 2006.
- 1119 Wang, K., Zhang, Y., Yahya, K., Wu, S.-Y., and Grell, G.: Implementation and initial application
1120 of new chemistry-aerosol options in WRF/Chem for simulating secondary organic aerosols and
1121 aerosol indirect effects for regional air quality, *Atmos. Environ.*, 115, 716–732,
1122 <https://doi.org/10.1016/j.atmosenv.2014.12.007>, 2015.
- 1123 Wang, K., Zhang, Y., Zhang, X., Fan, J., Leung, L. R., Zheng, B., Zhang, Q., and He, K.: Fine-scale
1124 application of WRF-CAM5 during a dust storm episode over East Asia: Sensitivity to grid
1125 resolutions and aerosol activation parameterizations, *Atmos. Environ.*, 176, 1–20,
1126 <https://doi.org/10.1016/j.atmosenv.2017.12.014>, 2018.
- 1127 Wang, K., Zhang, Y., Yu, S., Wong, D. C., Pleim, J., Mathur, R., Kelly, J. T., and Bell, M.: A
1128 comparative study of two-way and offline coupled WRF v3.4 and CMAQ v5.0.2 over the
1129 contiguous US: performance evaluation and impacts of chemistry–meteorology feedbacks on
1130 air quality, *Geosci. Model Dev.*, 14, 7189–7221, <https://doi.org/10.5194/gmd-14-7189-2021>,
1131 2021.
- 1132 Wang, S. and Hao, J.: Air quality management in China: Issues, challenges, and options, *J. Environ.*
1133 *Sci.*, 24, 2–13, [https://doi.org/10.1016/S1001-0742\(11\)60724-9](https://doi.org/10.1016/S1001-0742(11)60724-9), 2012.
- 1134 Wang, Z., Wang, Z., Li, J., Zheng, H., Yan, P., and Li, J.: Development of a meteorology-chemistry
1135 two-way coupled numerical model (WRF-NAQPMS) and its application in a severe autumn
1136 haze simulation over the Beijing-Tianjin-Hebei area, China. *Clim. Environ. Res.*, 19, 153–163,
1137 <https://doi.org/10.3878/j.issn.1006-9585.2014.13231>, 2014.
- 1138 Womack, C. C., Manfred, K. M., Wagner, N. L., Adler, G., Franchin, A., Lamb, K. D., Middlebrook,
1139 A. M., Schwarz, J. P., Brock, C. A., and Brown, S. S.: Complex refractive indices in the
1140 ultraviolet and visible spectral region for highly absorbing non-spherical biomass burning
1141 aerosol, *Atmos. Chem. Phys.*, 21, 7235–7252, <https://doi.org/10.5194/acp-21-7235-2021>, 2021.
- 1142 Wong, D. C., Pleim, J., Mathur, R., Binkowski, F., Otte, T., Gilliam, R., Pouliot, G., Xiu, A., Young,
1143 J. O., and Kang, D.: WRF-CMAQ two-way coupled system with aerosol feedback: software
1144 development and preliminary results, *Geosci. Model Dev.*, 5, 299–312,
1145 <https://doi.org/10.5194/gmd-5-299-2012>, 2012.
- 1146 Wu, Y., Cheng, T., Liu, D., Allan, J. D., Zheng, L., and Chen, H.: Light absorption enhancement of
1147 black carbon aerosol constrained by particle morphology, *Environ. Sci. Technol.*, 52, 6912–



- 1148 6919, <https://doi.org/10.1021/acs.est.8b00636>, 2018.
- 1149 Xie, B., Fung, J. C. H., Chan, A., and Lau, A.: Evaluation of nonlocal and local planetary boundary
1150 layer schemes in the WRF model, *J. Geophys. Res. Atmos.*, 117,
1151 <https://doi.org/10.1029/2011JD017080>, 2012.
- 1152 Xing, J., Wang, J., Mathur, R., Wang, S., Sarwar, G., Pleim, J., Hogrefe, C., Zhang, Y., Jiang, J.,
1153 and Wong, D. C.: Impacts of aerosol direct effects on tropospheric ozone through changes in
1154 atmospheric dynamics and photolysis rates, *Atmos. Chem. Phys.*, 17, 9869–9883,
1155 <https://doi.org/10.5194/acp-17-9869-2017>, 2017.
- 1156 Xu, D., Ge, B., Chen, X., Sun, Y., Cheng, N., Li, M., Pan, X., Ma, Z., Pan, Y., and Wang, Z.: Multi-
1157 method determination of the below-cloud wet scavenging coefficients of aerosols in Beijing,
1158 China, *Atmos. Chem. Phys.*, 19, 15569–15581, <https://doi.org/10.5194/acp-19-15569-2019>,
1159 2019.
- 1160 Zhang, S., Sarwar, G., Xing, J., Chu, B., Xue, C., Sarav, A., Ding, D., Zheng, H., Mu, Y., and Duan,
1161 F.: Improving the representation of HONO chemistry in CMAQ and examining its impact on
1162 haze over China, *Atmos. Chem. Phys.*, 21, 15809–15826, <https://doi.org/10.5194/acp-21-15809-2021>, 2021.
- 1164 Zhang, Y.: Online-coupled meteorology and chemistry models: history, current status, and outlook,
1165 *Atmos. Chem. Phys.*, 8, 2895–2932, <https://doi.org/10.5194/acp-8-2895-2008>, 2008.
- 1166 Zhang, Y., Zhang, X., Wang, K., Zhang, Q., Duan, F., and He, K.: Application of WRF/Chem over
1167 East Asia: Part II. Model improvement and sensitivity simulations, *Atmos. Environ.*, 124, 301–
1168 320, <https://doi.org/10.1016/j.atmosenv.2015.07.023>, 2016.
- 1169 Zhao, B., Liou, K., Gu, Y., Li, Q., Jiang, J. H., Su, H., He, C., Tseng, H.-L. R., Wang, S., and Liu,
1170 R.: Enhanced PM_{2.5} pollution in China due to aerosol-cloud interactions, *Sci. Rep.*, 7, 1–11,
1171 <https://doi.org/10.1038/s41598-017-04096-8>, 2017.
- 1172 Zheng, B., Zhang, Q., Zhang, Y., He, K. B., Wang, K., Zheng, G. J., Duan, F. K., Ma, Y. L., and
1173 Kimoto, T.: Heterogeneous chemistry: a mechanism missing in current models to explain
1174 secondary inorganic aerosol formation during the January 2013 haze episode in North China,
1175 *Atmos. Chem. Phys.*, 15, 2031–2049, <https://doi.org/10.5194/acp-15-2031-2015>, 2015.
- 1176 Zhou, C., Zhang, X., Gong, S., Wang, Y., and Xue, M.: Improving aerosol interaction with clouds
1177 and precipitation in a regional chemical weather modeling system, 16, 145–160,
1178 <https://doi.org/10.5194/acp-16-145-2016>, 2016.
- 1179 Zhu, J., Wang, S., Wang, H., Jing, S., Lou, S., Saiz-Lopez, A., and Zhou, B.: Observationally
1180 constrained modeling of atmospheric oxidation capacity and photochemical reactivity in
1181 Shanghai, China, *Atmos. Chem. Phys.*, 20, 1217–1232, <https://doi.org/10.5194/acp-20-1217-2020>, 2020.
- 1183 Zhu, J., Chen, L., Liao, H., Yang, H., Yang, Y., and Yue, X.: Enhanced PM_{2.5} decreases and O₃
1184 increases in China during COVID-19 lockdown by aerosol-radiation feedback, *Geophys. Res.
1185 Lett.*, 48, 1–11, <https://doi.org/10.1029/2020GL090260>, 2021.
- 1186